Snowdrift-permitting simulations of seasonal snowpack processes over large extents

Christopher B. Marsh[1,2], Zhibang Lv[1,2], Vincent Vionnet[4,2], Phillip Harder[1,2], Raymond J. Spiteri[3,2], and John W. Pomeroy[1,2]

[1] Centre for Hydrology, University of Saskatchewan, Canada
[2] Global Institute for Water Security, University of Saskatchewan, Canada
[3] Numerical Simulation Lab, University of Saskatchewan, Canada
[4] Meteorological Research Division, Environment and Climate Change Canada

1 Abstract

The melt of seasonal snowpack in mountain regions provides downstream river basins with a critical supply of freshwater. Snowdrift-permitting models (1 m – 250 m) have been proposed as a way to accurately simulate snowpack heterogeneity that stems from differences in energy inputs, over-winter redistribution, sublimation, melt, and variations in precipitation. However, these spatial scales can be computationally intractable for large extents. In this work, the multiscale Canadian Hydrological Model (CHM) was applied to simulate snowpacks at snowdrift-permitting scales (≈ 50 m) across the Canadian Cordillera and adjacent regions (1.37 million km^2) forced by downscaled atmospheric data. The use of a multiscale land surface representation resulted in a reduction of computational elements of 98% while preserving land-surface heterogeneity. CHM includes complex terrain windflow and radiative transfer calculations, lapses temperature, humidity, and precipitation with elevation, redistributes snow by avalanching, wind transport and forest canopy interception and calculates the energetics of canopy and surface snowpacks. Model outputs were compared to a set of multiscale observations including snow-covered area (SCA) from Sentinel and Landsat imagery, snow depth from uncrewed aerial system lidar, and point surface observations of depth and density. Including snow redistribution and sublimation processes improved the summer SCA r^2 from 0.7 to 0.9. At larger scales, inclusion of snow redistribution processes delayed full snowpack ablation by an average of 33 days, demonstrating process emergence with scale. These simulations show how multiscale modelling can improve snowpack predictions to support prediction of water supply, droughts, and floods.

2 Key points

- Large extent, snowdrift permitting scale simulation of ≈ 1.4M km^2
- Inclusion of snow redistribution was scale emergent and delayed full ablation by 33 days on average
- Inclusion of snow redistribution processes improved summer SCA r^2 from 0.7 to 0.9

3 Introduction

The melt of seasonal snow covers in regions provides vast downstream regions with a critical supply of freshwater (Sturm et al., 2017), impacting ecosystems and agricultural, industrial, and municipal users (Nazemi et al., 2013). Late-lying snowpacks can persist from spring melt through summer in mountain headwaters (Marsh et al., 2012; Hatchett, 2021), supporting mountain glaciers (Mott et al., 2019), and can maintain streamflow to vast downstream regions through periods of low precipitation (Jenicek et al., 2016). Globally, over one-sixth of the world's population lives in snow-dominated areas (Barnett et al., 2005), and an estimated close to two billion people depend on mountain runoff contributions (Viviroli et al., 2020; Adler et al., 2022). There is an urgent need to improve the predictions of mountain snowpacks to aid in water supply forecasts for downstream floods, hydroelectricity generation, irrigated agriculture withdrawals, ecosystem management, reservoir management, ecotourism, and drinking water supply (Arnal et al., 2023).

The substantial spatial and temporal variability of mountain snowpacks is predominately due to the impact of blowing-snow redistribution (Pomeroy et al., 1993; MacDonald et al., 2009; MacDonald et al., 2010; Mott et al., 2010; Vionnet et al., 2014; Mott et al., 2018; Marsh et al., 2020a; Vionnet et al., 2021b) that can lead up to 30% to 40% of the areal snowpack being lost to in-transit sublimation (Mott et al., 2018). The redistribution of snow from the windward to the leeward slopes, valley bottoms, gullies, and tree-lines creates highly heterogeneous snowpacks (Pomeroy et al., 2003) that can be redistributed to lower elevations by avalanches (Bernhardt and Schulz, 2010). Avalanches redistribute snow from high-elevation, low-melt-rate locations to low-elevation, potentially high-melt-rate locations, creating areas of high snow water equivalent (SWE), and persistent snowcover (Bernhardt and

Schulz, 2010). Nestled at the base of steep slopes, some of these locations can be highly shaded (Marsh et al., 2012), allowing avalanche deposits to persist late into the summer months. They may also not melt and thus support glacial ice formation (Mott et al., 2019; Pradhananga and Pomeroy, 2022). In forested locations, snow is intercepted by canopies, where it can be redistributed by wind and gravity, and is subject to sublimation and melt (Pomeroy et al., 1998; Lundquist et al., 2021; Lumbrazo et al., 2022), resulting in over-winter ablation of 20-40% of seasonal snowfall (Pomeroy and Gray, 1995; Essery and Pomeroy, 2004).

Snowpack heterogeneity is compounded during the ablation period where snow ablation rates differ by orders of magnitude (Pomeroy et al., 2003; DeBeer and Pomeroy, 2010; Ellis et al., 2013). Slope, aspect, and shading impact shortwave irradiance (Marsh et al., 2012) and longwave irradiance (Sicart et al., 2006). Wind exposure impacts differences in turbulent transfer of scalar fluxes (Pomeroy et al., 2003; Reba et al., 2009; Conway et al., 2018). The effect of forest canopies further magnifies the impact of suppressing turbulent transfer (Harding and Pomeroy, 1996), attenuating shortwave irradiance (Pomeroy et al., 2007) and enhancing longwave irradiance (Pomeroy et al., 2009). This suppression results in much slower mountain snowmelt under evergreen forest canopies than in adjacent open areas (Marks and Winstral, 2001; Ellis et al., 2013).

Observation of mountain SWE is highly uncertain due to the substantial heterogeneity of mountain snowpacks, inaccessible terrain, remoteness from roads, and large spatial areas. The locations of manual snow course observations and automated point observations of snow depth and SWE are often biased to mid- and low-elevation locations (Brown and Braaten, 1998; DeBeer et al., 2016), and they typically do not capture the full snowpack heterogeneity in a basin or region. Due to avalanche-prone or dangerous terrain, these observations typically miss key areas of a mountainous watershed such as cornices, avalanche deposits, ridges, and steep slopes (Brown and Braaten, 1998; Vionnet et al., 2021a).

Remote-sensed observation of snow depth and cover from satellites, aircraft, and Uncrewed Aerial Systems (UAS) has significantly improved in availability and fidelity over the past 20 years (Deems et al., 2013; Tedesco et al., 2014; Harder et al., 2016; Painter et al., 2016b). However, none of these methods can measure SWE reliably. Satellite-borne radar requires precise knowledge of *in situ* snow microstructure to constrain estimates of SWE (Rutter et al., 2019), and estimation of the spatial SWE heterogeneity is further complicated by the often-low spatial resolutions ($\approx$ 1 km). Passive microwave is at an even lower resolution ($>$ 10 km) (Tsang et al., 2022) and is extremely sensitive to snow microstructure such as wet snow, sub-canopy snow, or snowpacks with ice layers (Sandells et al., 2021). Structure from Motion (SfM) using UAS photography can estimate snow depth at high spatial resolutions ($\approx$ 0.1 m) in open areas over small spatial extents, but cannot be confidently applied where there is exposed vegetation (shrubs, forests) (Harder et al., 2016). The availability of more powerful UAS is now allowing for regular drone-based lidar acquisitions in both open and forested areas (Harder et al., 2020; Jacobs et al., 2021). However, the spatial coverage of these observations remains small (10 km^2). Airborne plane-based lidar observations cover larger areas than UAS (Chasmer et al., 2008; Hopkinson and Chasmer, 2009; Pelto et al., 2019), at the trade-off of lower-density point clouds, and high uncertainty for snow depth under dense forest canopies and on steep slopes. Constraining simulated snowdepth via assimilation techniques with lidar is successfully used in an operational context in the Sierra Nevada, USA, over important water supply river basins ($\approx$ 1000 km^2) to provide water managers with the evolution of alpine snow depth and an end-of-winter snow water equivalent (SWE) (Painter et al., 2016b). Unfortunately, the large extent application of airborne lidar remains limited due to high operational expenses. This cost is compounded when considering the size and difficult conditions of global mountain ranges. Satellite laser altimetry such as ICESat-2 provides high-resolution elevation datasets, however, in steep mountain slopes the vertical accuracy creates high uncertainty (Deschamps-Berger et al., 2022). In all cases, snow depth observations require some form of a modelled estimate of snow cover density to derive a SWE estimate.

First-principles mass-energy balance conservation approaches tend to improve simulations in cold regions versus empirical schemes such as degree-day, e.g., Marsh and Pomeroy (1996); Bartelt and Lehning (2002); Bowling et al. (2004); Etchevers et al. (2004); Raderschall et al. (2008); Dornes et al. (2008); Ellis et al. (2010); Essery et al. (2009); Essery et al. (2013); Pomeroy et al. (2012); Fang et al. (2013); Kumar et al. (2013); Endrizzi et al. (2014); Mosier et al. (2016); Painter et al. (2016a); Harder et al. (2018). Such approaches encourage using physically measurable parameters where possible and landscape discretisations that explicitly represent observed landscape heterogeneity (Dornes et al., 2006; Pomeroy et al., 2007; Hrachowitz and Clark, 2017; Pomeroy et al., 2022). Snowdrift-permitting length scales (1 m – 250 m) have been proposed as needed to accurately simulate snow cover heterogeneity (Vionnet et al., 2021b). Such scale requirements generally imply using explicitly distributed models. Although Hydrological Response Unit (HRU) (Flügel, 1995) models have had success in alpine terrain (DeBeer and Pomeroy, 2010; Fang et al., 2013; Aubry-Wake et al., 2022; Pradhananga and Pomeroy, 2022), a ‘sufficient’ number

of HRUs must be used to avoid a regression-towards the mean characteristic due to the lumped HRU nature, which may be counterproductive over large spatial extents by resulting in a distributed lumped model. It is often (erroneously) assumed that computational constraints limit the applicability of explicitly distributed models that incorporate key processes such as blowing snow transport and sublimation, forest canopy interception, melt, unloading, and sublimation, and snow avalanches. As a result, a reduction in computational requirements occurs via a combination of smaller spatial extents, coarser spatial or temporal resolution, and neglected processes. These simplifications may lead to poor predictive capacity and impose an unnecessary need for calibration of model parameters to fit sparse, and often unrepresentative, observations of snow accumulation and ablation.

A solution is to use multiscale land surface models that allow for large reductions in computational elements while preserving critical land-surface heterogeneity and comprehensive snow processes. In this work, the multiscale Canadian Hydrological Model (CHM) (Marsh et al., 2020b) was applied to simulate snow covers at snowdrift-permitting scales across the Canadian Cordillera (1.37 million km^2) driven with down scaled meteorological forcing from the Environment Canada High Resolution Deterministic Prediction System (HRDPS) at a spatial resolution of 2.5 km. A multiscale evaluation approach was used. The model outputs were compared to indices of the snow-covered area using Sentinel and Landsat imagery, high-resolution, small-extent lidar observations of snow depth, and point-scale observations of SWE and snow depth. This is the first large-extent application of a deterministic, non-calibrated comprehensive snow redistribution and ablation model that includes a rigorous quantification of cold regions processes at snowdrift resolving scales ($\approx$ 50 m). Such an approach presents a direction for supporting improved prediction of water supply, droughts, and floods, including land cover and climate changed. Specifically, this manuscript aims to investigate the following questions: 1) Can a deterministic, non-calibrated snowdrift permitting model be applied to large spatial extents?; 2) Can such a model estimate late lying snowpacks well?; 3) What are the implications of neglecting redistribution processes on regional scale snowpacks and SCA?

4 Study domain

The simulation domain, shown in Figure 1, is a region from 46N to 55N and 109W to 132W, covering an area of approximately 1.37M km^2. Six regional domains are shown, with boundaries in white: Coastal, Interior/Prairies, and Rockies/Foothills for the United States (US) and Canada (CAN), split at the US-CAN border. The domain extends from the Saskatchewan–Alberta border westward to the Pacific Ocean, and from north-central British Columbia southward to northern Washington state, Idaho, and Montana. The domain spans an elevation range from 0 m to 4413 m and covers areas of high topographic relief, lowlands, prairies, seasonal snow covers, and glaciers. The entirety of the Fraser River basin is included, as are the headwaters of the Columbia, Saskatchewan, Missouri, and the Mackenzie River Basins – rivers flowing to the Atlantic, Arctic, and Pacific oceans. These basins derive the majority of their streamflow from seasonal snow covers and glaciers (Whitfield et al., 2021). This region covers the Pacific Maritime, semi-arid plateaux, Montane Cordillera, and Boreal plains (Whitfield et al., 2021). The Continental Divide, which follows the British Columbia (left-most province) and Alberta (middle province) border, is an important topographic boundary. East of this divide, the mountain region provides fresh water to the Canadian Prairies, home to 80% of Canada's irrigated agriculture production (Whitfield et al., 2021).

The West-to-East transition is one from a maritime to a cold continental climate. The western, maritime Coast Mountains are dominated by highly varying slopes of forested and alpine terrain, ranging from 0 m to over 3000 m (Sobie and Murdock, 2021). Annual precipitation in this region varies from 200 mm to over 5000 mm, primarily falling between November and January (Sobie and Murdock, 2021). East of the dry and warm interior plateau, precipitation increases dramatically towards the Continental Divide (DeBeer et al., 2015). In the Rockies, winters are cold and dominated by continental air masses and the easternmost slopes are frequently impacted by Chinook winds (Foehns) (MacDonald et al., 2018). Low elevations are dominated by coniferous forests and alpine terrain is dominated by tundra shrubs, talus, and exposed bedrock (DeBeer et al., 2015). Low-elevation mean winter temperatures range from -10 ºC to -15 ºC, and high-elevation temperatures are much lower (DeBeer et al., 2015).

5 Model description

The water year 2021 (Oct 1, 2020–Oct 1, 2021) was simulated at a 1-hour time step for the region described above. Two model realizations, with and without redistribution (blowing snow and avalanches), were compared. The numerical model is detailed below.

5.1 CHM

The Canadian Hydrological Model (CHM) (Marsh et al., 2020b) was used to perform the simulations. CHM is a flexible, modular, multiscale modelling framework based on the unstructured triangular meshes described later in Section 8. It is a spatially explicit distributed model that incorporates the key processes of cold-regions snow hydrology. To date, development in CHM has focused on the surface snow processes, with hydrological processes to be added in an upcoming release. CHM can use distributed numerical weather predictions (NWP) as meteorological forcing inputs, which are down-scaled to the triangular model elements. This process is described in detail in Section 9. The parameterisations used follows the previous application of CHM to mountain terrain (please refer to the detailed description in Marsh et al. (2020a); Vionnet et al. (2021b); Marsh et al. (2020b)), and key processes are briefly summarized below. Lakes were masked out — a lake module will be added in a future CHM release. Lastly, although the simulation domain covers a portion of the Pacific Ocean and large lakes, no open water processes were simulated.

5.2 Snow Model

Newly added to CHM is the intermediate complexity FSM2 snowpack model (Essery, 2015; Mazzotti et al., 2020b). FSM and FSM2 have been used across a diverse set of landscapes including mountain, forested, and open sites (Krinner et al., 2018; Mazzotti et al., 2020b, 2020a; Mott et al., 2023). It explicitly resolves the energy and mass balance fluxes between the atmosphere and snowpack, including the turbulent and latent heat fluxes, long and shortwave radiation fluxes, and ground heat flux. It uses a three-layer numerical discretization of the snowcover with minimum layer thicknesses (enumerated top-to-bottom) of 0.1 m, 0.2 m, and 0.4 m. Unlike SNOWPACK (Bartelt and Lehning, 2002), FSM2 does not explicitly simulate snow microstructure. Although available in multi configuration options (Essery, 2015; Mazzotti et al., 2020b), the configuration used in CHM is the most detailed, physically complete variant, including a Monin-Obukov stability adjustment and a linear snow cover fraction. The CHM configuration does not currently include the advanced canopy parameterization of Mazzotti et al. (2020b) and Mazzotti et al. (2020a).

5.3 Vegetation Canopy

Each computational element was partitioned into open and forested areas based on the vegetation database described in Section 7.2. The snow interception parameterization of Hedstrom and Pomeroy (1997) was coupled with the snow sublimation and unloading parameterization of Pomeroy et al. (1998) and Ellis et al. (2010). Sub-canopy wind and radiation transfer is via the method described in Ellis et al. (2010).

5.4 Snow Redistribution

Blowing-snow redistribution and sublimation were estimated using the Prairie Blowing Snow Model 3D (PBSM3D) (Marsh et al., 2020a), a formulation of PBSM (Pomeroy et al., 1993; Pomeroy and Li, 2000) designed for variable-resolution meshes. Despite the name, PBSM has been successfully applied to mountain domains, e.g., MacDonald et al. (2010); Krogh et al. (2015); Musselman et al. (2015a); Marsh et al. (2020a); Vionnet et al. (2021b). The PBSM3D formulation discretizes a steady-state advection-diffusion formulation of PBSM on the triangular mesh with vertical layers, resulting in 3D control volumes. Upwind fetch is computed via the method from Lapen and Martz (1993) adopted for variable-resolution meshes. Avalanches are estimated using SnowSlide (Bernhardt and Schulz, 2010), which is an empirical snow depth–slope threshold parameterization. SnowSlide is not intended for hazard forecasting. Rather, it is used to redistribute high-elevation snow to lower elevations. SnowSlide was originally calibrated in the Alps with no adjustments; here, the parameter values reported in Bernhardt and Schulz (2010) were used directly as detailed in Vionnet et al. (2021b).

5.5 Model Outputs

For comparison with existing evaluation raster data, the numerical model outputs were regridded from the variable-resolution unstructured mesh to a fixed-resolution raster, 0.0007° x 0.0007° (≈ 50 m x 50 m). This regridding was done using the Earth System Modelling Framework (ESMF) software v8.4 (https://earthsystemmodeling.org/) using the bilinear regridder.

6 High-performance computing advances

To allow for the application of CHM over such a large spatial extent at snowdrift-permitting scales with the full suite of physics-based redistribution parameterizations, significant advances in the high-performance computing capabilities of CHM were required. These advances extend the originally described CHM v1.0 in Marsh et al. (2020b). Four key innovations were required: 1) implementation of the Message Passing Interface (MPI) to distribute the computations across multiple compute nodes; 2) a domain decomposition to split the computations in space; 3) implementation of a global, parallel linear algebra solver; and 4) an improved MPI-aware avalanche model. These advances are described below.

6.1 Implementation of MPI

The incorporation of the Message Passing Interface (MPI) into CHM augmented the existing thread-parallel OpenMP parallelism, as described in Marsh et al. (2020b). The parallelism via OpenMP performed parallelism across the set of triangle faces. Now, the domain is decomposed into n subdomains, one for each MPI rank, and the triangles within that rank are iterated over in parallel with OpenMP. Each MPI rank can run on multiple computational nodes. Per-rank file input and output is now performed, improving a major serial bottleneck. The domain decomposition for MPI is described below.

6.2 Domain Decomposition

In a raster-based model, domain decomposition is natural — the array that describes the raster domain is split into n chunks, one for each MPI rank. This trivially ensures that computational elements (i.e., raster cells) that are close in space are close in memory. This is not the case for unstructured meshes. Similar to rasters, the triangles have a globally unique identification number (global ID) that monotonically increases from 0 to the number of triangles in the mesh. Because the mesh is the product of a Delaunay triangulation algorithm (Marsh et al., 2018), the triangle global IDs are not monotonically increasing when traversed in a neighbour-to-neighbour fashion (i.e., breadth- or depth-first searches). That is, triangles that are close in space (i.e., adjacent) may not be close in memory. To illustrate this, consider the example shown in Figure 2, where there are four MPI ranks (coloured green, blue, red, and white) that divide the T triangles between ranks. Thus, any parallel distribution of these triangles results in a suboptimal distribution of triangles across the MPI ranks, leading to an overhead of MPI triangle-to-triangle communications.

A solution is to use a domain-partitioning strategy that reorders the triangles such that triangles close in space are also close in memory. This is done via the serial graph partition and fill-reducing matrix ordering of METIS (Karypis and Kumar, 1998). In addition, the fill-reducing ordering produced by METIS reduces the computational and storage requirements of sparse matrix factorization (Karypis and Kumar, 1998), places the non-zero elements closer to the diagonal, and enhances data locality (Azad et al., 2017). These are important attributes for CHM because the matrix representation of PDE discretisations is always sparse. It is critical to note that although METIS often produces contiguous partitions, it is not guaranteed to produce spatially contiguous partitions. Because the underlying structure of CHM makes no assumptions about the unstructured mesh topology, it can thus represent both the naive decomposition shown in Figure 2 and the optimized METIS decomposition. Other partition strategies were explored, including the Reverse Cuthill-Mckee (RCM; Cuthill and McKee (1969)). However, the RCM partition resulted in many long and thin partitions, which resulted in significantly increased MPI communication overhead for lateral flux redistribution due to frequent crossing of multiple MPI domains. This was especially noticeable for the domain in Figure 1, where a partition would run the full east-to-west length of the domain but would only be a handful of triangles tall.

The resulting domain decomposition for 448 ranks is shown in Figure 3. Each colour corresponds to one of the 448 MPI ranks; however, colours are reused. Although these partitions may look like hydrological basins, they are not. Because of the variable area of the triangles, each partition has approximately the same number of triangles.

6.3 Ghost Triangles

Additional complexities are associated with the domain decomposition that must be addressed. First, because CHM simulates horizontal mass redistribution, a horizontal mass flux must be supported. This requires that triangles can communicate with their neighbours either for building a sparse matrix representation, e.g., blowing snow, or for

explicitly exchanging mass, e.g., avalanches. This is done by the traditional ghost neighbour approach (herein type I ghosts) and a ghost neighbour region for topographic queries (herein type II ghosts).

Type I ghosts are directly adjacent to the MPI rank's bounding triangles. These ghosts are used to calculate "up-wind" (in the numerical sense) fluxes to use as a boundary condition and can directly communicate with other MPI ranks. For example, with the blowing snow flux, type I ghosts are used to compute an up-wind (numerical and physical sense) blowing snow flux into the domain and a down-wind flux for mass exiting the domain. Examples of type I ghosts are shown in Figure 4 (a) as coloured triangles for one of the domain partitions described above. The colours correspond to the rank with which a given triangle is communicating. A zoomed-in section is shown in Figure 4 (b), where the overlapping triangles for MPI rank 1 (hollow fill) are shown.

Type II ghosts are used for querying landscape elements farther away than type I ghosts. In spatially explicit earth system models, there are frequent queries from a model element about the surrounding topography. For example, this may be to calculate fetches or terrain shadowing. Thus, type II ghosts exist as part of the domain to be used in the algorithms without the need to query other MPI ranks for their domain's physical characteristics. In practice, this reduction in querying results in a substantial improvement to model runtime, despite the increase in complexity required to coordinate the two types of ghost faces. Examples of type II ghosts are shown in Figure 5, (a) where type I ghosts are shown in orange and type II ghosts for a 1000 m distance are shown in purple. Figure 5 (b) shows a zoomed-in region. The neighbour partition is shown as hollow triangles in both (a) and (b).

The domain partitioning and determination of ghost faces (both type I and type II) are pre-processing steps and are computed before the model run. Each partition is written to a separate file. This allows for a single file to be loaded per MPI rank, allowing for reduced memory usage. In addition, the pre-processing tool developed allows for isolating individual partitions and writing those individually. This enables only that portion of the mesh to be loaded, allowing for simpler debugging on subsets of the entire model domain.

6.4 PBSM3D Solver Improvement

The existing ViennaCL (Rupp et al., 2016) shared-memory linear algebra solver introduced to CHM for solving the PBSM3D discretization in Marsh et al. (2020a) was replaced with the globally parallel sparse linear algebra Kokkos solver from the Trilinos project (Team, 2020 (acccessed May 22, 2020)). Trilinos is a set of scientific computing libraries developed for the United States Department of Energy. The use of this library allows each rank to fill in its portion of the sparse matrix, obtaining a globally valid solution via MPI. This ensures that mass fluxes that cross MPI ranks are correctly accounted for.

6.5 An Improved MPI-Aware Avalanche Scheme

CHM includes the vertical redistribution of snow via avalanches through the inclusion of the SnowSlide algorithm (Bernhardt and Schulz, 2010). SnowSlide was originally developed as a non-parallel algorithm. Therefore, it had to be modified to be applicable to the partitioned MPI approach described above. The SnowSlide algorithm, as originally written, begins at the highest point of the domain and sequentially redistributes a snowpack that exceeds some given depth on a terrain element with a minimum slope downhill. This procedure continues until no snow remains for redistribution. This algorithm has been converted to an iterative approach with an explicit MPI communication step. Whenever the snow is moved to a Type I ghost triangle, this amount is accumulated, and after all the triangles have moved mass, the Type I ghosts exchange the accumulated snow. The SnowSlide algorithm is then re-run with this newly added snow. This procedure continues until no snow is redistributed or a maximum set of iterations are exceeded, after which an approximately steady state is assumed. This process is summarized in Algorithm 1.

```
input  : A mesh Mesh
input  : A triangle's snowmass s
ghost  : TypeII ghost snowmass st
while not done do
    foreach tri in Sort(Mesh) do
        MoveMassDownhill(s, tri)
        if tri is Type I then
            st ← st + s
        end
    end
    MPIExchangeGhosts(st)
    if exceeds maxItr then
        done ← true
    end
    if st = 0 then
        done ← true
    end
end
```

Algorithm 1: The SnowSlide algorithm adapted for use with MPI parallelism.

7 Land surface Data

7.1 Elevation

The digital elevation model (DEM) used, shown in Figure 1, was the 1" (≈ 30 m) Forest And Buildings removed Copernicus DEM (FABDEM) (Hawker et al., 2022). This DEM is derived from the Copernicus GLO-30 (herein COP30) (AIRBUS, 2020) Digital Surface Model (DSM), a TanDEM-X X-band global radar dataset acquired between 2010 and 2015 (AIRBUS, 2020). The forest bias present in the COP30 DSM has been removed by using random forest machine learning to remove vegetation over 3 m in height and urban buildings (Hawker et al., 2022). A combination of global forest canopy height datasets was used as training data, including the Global Ecosystem Dynamics Investigation (GEDI) (Dubayah et al., 2020), the Global Forest Canopy Height 2019 data-set (Potapov et al., 2021), ICESat-2 (Ice, Cloud, and land Elevation Satellite) (Neuenschwander et al., 2021) laser altimetry canopy heights, and the Copernicus Global Land Service collection 3 epoch 2015 canopy coverage. The accuracy of this removal was evaluated in Marsh et al. (2023a) for the Canadian Rockies, where the FABDEM was compared against sub-canopy drone lidar elevation. It was found that FABDEM had a 24% reduction in RMSE and 135% reduction in bias compared to the COP30 DSM. This suggests that the DEM is well adapted for the simulation domain.

7.2 Vegetation

Land cover and vegetation type were obtained from the North American Land Change Monitoring System (NALCMS; Latifovic et al. (2016)). This is a joint initiative between American, Canadian, and Mexican environmental agencies (Colditz et al., 2012). The dataset is a harmonized land cover product derived from the Landsat and RapidEye images. For this work, the 2015 30 m spatial resolution RapidEye dataset was used. These data are shown in Figure 6. Urban classified areas were treated as "open".

7.3 Water Mask

The 2019-v1.7 data mask showing permanent water bodies from Hansen et al. (2013) was used. These data are derived from the 30 m Landsat 8 Operational Land Imager (OLI). The Hansen et al. (2013) water mask was used instead of the NALCMS inland-water mask due to also including the coastal regions. The water mask is shown as water (blue) in Figure 6.

8 Mesh Generation

An unstructured triangular mesh was created using the mesh generation software *Mesher* (Marsh et al., 2018) using the described datasets as input. Briefly, *Mesher* produces variable-resolution triangular meshes using multi-objective criteria to ensure triangles represent key landscape features such as topography and vegetation. It takes as input any secondary landscape rasters, such as vegetation type, to parameterize the triangles. That is, it regrids the raster data to the triangles. The resulting unstructured mesh is used as input to the numerical model, as described in Section 5.

The mesh generation followed the snowdrift-permitting scale of Vionnet et al. (2021b). The variable-resolution mesh generated had a minimum triangle area of 50 m x 50 m and a maximum vertical error, as measured by Root Mean Squared Error (RMSE) to the source raster DEM, of 15 m. The maximum triangle area was 2500 m x 2500 m. These criteria ensured a minimum of 50 m length scale around complex topography such as mountainous ridge lines. A secondary constraint on the mesh generation was the water mask to ensure water boundaries were well approximated. The mesh generation reduced the roughly 3 billion source elevation raster cells to approximately 34 million triangles, representing a 98.9% reduction in computational elements versus the input raster DEM. The resulting mesh is shown in Figure 7, where the source DEM is shown in colour and the unstructured mesh is overlain and shown in grey.

9 Atmospheric Forcing

Due to the sparse surface observations located mainly at low elevations across this study domain (DeBeer et al., 2021), the Environment and Climate Change Canada (ECCC) High Resolution Deterministic Prediction System (HRDPS; Milbrandt et al. (2016)) was used as atmospheric forcing input. The HRDPS is a high-resolution, 2.5 km NWP system running over Canada and the northern extents of the United States. Successive 24-hour forecasts issued at 00:00 UTC were combined to produce a continuous time series. Using NWP outputs to drive snowpack models is increasingly common due to the requirement of many input variables (Quéno et al., 2016; Havens et al., 2019; Vionnet et al., 2021b). Using NWP outputs can be advantageous because they overcome the bias due to observation sites being preferentially located in valley bottoms or near airports (DeBeer et al., 2021). In complex topography, they can better capture atmospheric flows (Quéno et al., 2016, 2018; Lundquist et al., 2019; Vionnet et al., 2021b).

The 2.5 km HDRPS data were downscaled to the model elements (triangles) during model runtime. Horizontal interpolation using the closest four HRDPS grid points was done via inverse-distance weighting (IDW). Elevation corrections to account for the difference between the model's computational element elevations and the HRDPS interpolated elevation were then applied. HRDPS 2-m air temperature and relative humidity were corrected via constant monthly lapse rates (Kunkel, 1989; Shea et al., 2004). The down-scaled temperature and humidity were used to estimate the precipitation phase via the psychrometric energy balance method of Harder and Pomeroy (2013). HRDPS direct and diffuse solar irradiance were corrected for slope and aspect as described in Marsh et al. (2012) with topographic shadowing computed via Dozier and Frew (1990) adapted for unstructured meshes (Marsh et al., 2020b). Longwave irradiance was adjusted for elevation difference using the climatological lapse rate of Marty et al. (2002). Lastly, the HRDPS 40-m wind speed and direction were downscaled to the CHM mesh using *Windmapper* (Marsh et al., 2023b). Windmapper uses the diagnostic windflow model WindNinja (Wagenbrenner et al., 2019) to produce a library of wind velocity perturbations to approximate the mechanical impact of terrain on windflow. An approximation to the leeside windspeed slowdown is done via the *Sx* method (Winstral et al., 2009) as described in Vionnet et al. (2021b) and Marsh et al. (2023b).

The HRDPS precipitation was not corrected for elevation because it was assumed that the HRDPS precipitation field already captured the main orographic effecting mountain precipitation (Lundquist et al., 2019). Commonly used precipitation–elevation corrections, such as that of Liston and Elder (2006), have been previously tested with CHM in the eastern Rockies; however, it led to a substantial overestimation of snow depth at high elevations. Precipitation amounts were corrected via a cosine correction to account for precipitation falling on an inclined model element (Kienzle, 2011). No additional precipitation bias correction was done. The creation of a distributed HRDPS

precipitation bias correction over multiple climatological regions for multiple years is outside the scope of this work. Advances in NWP systems have improved the precipitation estimate over mountain regions, e.g., Lundquist et al. (2019), and it is from further advances that better precipitation estimates will be made — not bespoke, one-off bias corrections relying on highly uncertain observations (Rasmussen et al., 2012). Thus, the precipitation is used as a best-effort estimate of precipitation in this area, cognizant that some precipitation bias likely remains and that it is representative of forecast systems in this region.

10 Evaluation Data and Metrics

Evaluating a distributed model over this large spatial extent is difficult. Evaluation points are spatially sparse and are at a different spatial scale than that of a model element. Spatial datasets derived from remotely sensed products have limited coverage in time and space. Despite these difficulties, a multiscale evaluation approach is detailed to diagnose the model behaviour. This approach uses observational datasets at different spatial scales, including remote sensed data and *in situ* point observations. These are used in both qualitative and quantitative comparisons. The spatial evaluation domain focused on the mountainous regions, where this classification followed Kapos et al. (2000) and shown in Figure 8. These classes are based on elevation and slope and were derived at 1 km resolution (Kapos et al., 2000). The following K1 elevation breaks were used: 0 m, 500 m, 1000 m, 1500 m, 2500 m, and 3500 m.

10.1 Point Observations

Point observations of SWE and depth were available from the CanSWE (Vionnet et al., 2021a) and SNOTEL (Yan et al., 2018; Sun et al., 2019) datasets. CanSWE gathers SWE measurements across Canada from provincial and territorial data providers, as well as universities and private companies such as hydropower companies. SNOTEL are bias and quality-controlled SWE and metrological datasets from automatic stations across the western United States and Alaska collected by the U.S. Department of Agriculture Natural Resources Conservation Service. The CanSWE and SNOTEL datasets were subset for October 1, 2020 to October 1, 2021 for all stations located within the simulation mountain domain (K1 region shown in Figure 8) that had at least 10 observation samples, limiting the selection to automatic measurements. The stations used for SWE are shown as white dots in Figure 1. Because of the subsetting done to the data, the station-basin hypsometry may be biased. A comparison (not shown) between the elevation distributions for CanSWE observations and the simulation DEM, segmented by the regional boundaries as shown in Figure 1, was done. The subset CanSWE observations had a reasonable hypsometry coverage with the simulation elevation with the subset-CanSWE mean elevation consistently at the upper interquartile range (IQR) of the DEM distribution, showing a slight high-elevation bias. However, the subset-CanSWE dataset entirely missed the DEMs high elevations. In the Interior CAN, the low elevations were not represented.

The differences between the simulated (S) and observed (O) results were evaluated using Mean Bias (MB) and Root Mean Squared Error (RMSE) as

$$\mathrm{MB} = \frac{1}{n}\sum_{i=1}^{n}(\mathrm{S}_i - \mathrm{O}_i) \qquad (1)$$

and

$$\mathrm{RMSE} = \sqrt{\frac{\sum_{i=1}^{n}(\mathrm{S}_i - \mathrm{O}_i)^2}{n}} \qquad (2)$$

where i is the sample number and n is the number of samples compared.

Using point observations to validate a spatial model is difficult due to the scale mismatch (Marsh et al., 2020a) and the incommensurability problem (Beven, 1989). This difficulty is exacerbated in mountainous forest domains, arising from the location of observations typically being in forest clearings which have anomalous energetics and redistribution features (Musselman et al., 2015b; Musselman and Pomeroy, 2016; Conway et al., 2018). Due to the combination of the larger 50 m to 2500 m length scales used in models and the coarse nature of land cover datasets (e.g., 30 m), there is a propensity for the model's spatial control volume to not represent these areas as clearings but as canopy or vice versa. That is, the model elements of these point locations correspond to the wrong land cover.

10.2 Snow Covered Area (SCA)

To evaluate the presence of snow on the ground, a combination of Landsat 8 and Sentinel-2 optical imagery was acquired for the evaluation period of Oct 1, 2020 to Oct 1, 2021 using Google Earth Engine (GEE). These images were harmonized to a common 50 m resolution via nearest-neighbour resampling, matching the same grid as the CHM raster output. Because of the large spatial extent of the simulation and evaluation domain, there were never any satellite passes that covered the entirety of the domain. Rather, swaths of the partial domain were covered. These swaths were masked for areas that were cloud free and non-treed using the 30-m tree mask of Hansen et al. (2013). Sentinel-2 imagery was masked using the S2 cloud probability cloud detector as implemented on GEE using all bands (https://developers.google.com/earth-engine/datasets/catalog/COPERNICUS_S2_CLOUD_PROBABILITY). The Landsat imagery was masked using the Landsat Simple Cloud Score (https://developers.google.com/earth-engine/apidocs/ee-algorithms-landsat-simplecloudscore) as implemented in GEE. This masking results in evaluation domains that change on a per-day basis, and an example of this is shown in red in Figure 9 for April 15, 2021. The per-day valid satellite coverage was used to mask the CHM model outputs. Therefore, these data represent a snapshot in space and time. The satellite-derived SCA observation data were compared to the simulated CHM on a gridcell-by-gridcell basis daily, and the MB and RMSE were computed. The normalized difference snow index (NDSI; Hall et al. (1995)) was calculated for the masked optical images. A binary snow/no-snow classification was conducted using an NDSI threshold of 0.4, where pixels with an NDSI value greater than 0.4 were classified as snow-covered and those with a value lower than or equal to 0.4 were classified as snow-free. To compare to CHM output, the end-of-day CHM SWE was thresholded for cells with SWE $\geq$ 5 mm to be considered as snow covered.

10.3 UAS-lidar Snow Depth

A high spatial resolution dataset of snow depth derived from UAS-lidar for May 4, 2021, was utilized from the Fortress Mountain Research Basin, a high elevation alpine-subalpine instrumented basin that is part of the Global Water Futures Observatories in the Canadian Rockies. Differencing between a snow free survey from September 18-19, 2018 and a snow-covered survey on May 4, 2021 provides a 1-m resolution dataset over a 4.8-km^2 extent of this headwater basin. The survey area includes exposed alpine ridgelines, sub-alpine forests, and montane meadows. The snow-free survey data were collected with a Riegl minvUX1-UAV lidar with an integrated APX-15 Inertial Measurement Unit (IMU) mounted on a DJI M600 UAV while the snow-covered survey was collected with a Riegl miniVUX2-UAV, with an integrated APX-20 IMU mounted on a FreeFly ALTA X UAV. Both systems were flown in a terrain following flight profile at 110 m above the surface. The data processing workflow is described in Harder et al. (2020). Absolute positioning was provided from a Lecia GS14 and 16 (respective to surveys) base station logging throughout the survey durations within the flight area and post-processing with the Leica Infinity (v 3.0.1.3069) software and precise point positioning from the NRCAN PPP system (Canada, n.d.). Post-processing of the IMU trajectory data was performed with the Applanix POSPAC UAV software (v 8.7), while the lidar processing utilized the proprietary Riegl data processing software (RiProcess v.1.9.2.4). Raw point clouds were processed with the LAStools software library (Isenburg, n.d.) to extract the respective ground and snow surfaces and rasterization to 1 m digital terrain and snow surfaces. Snow depth accuracy was assessed with respect to 44 manual snow depth observations that were surveyed with a GS16 real-time kinematic (RTK) rover survey and showed a RMSE of 0.23 m and MB of -0.03 m.

10.4 Basin- and Regional-Scale aggregation impacts

To evaluate how the impacts of snow redistribution and associated sublimation processes upscale to river basins and regions, the MERIT (Yamazaki et al., 2019) basins were used to aggregate the gridded model output. The MERIT basins were labelled with the broad region names shown in Figure 1. The simulated SWE was aggregated to the MERIT basins using the *exactextract* software (github.com/isciences/exactextract) to compute the spatial mean (μ) and spatial standard deviation (σ) of SWE for each MERIT hydrological basin. The spatial variability of SWE within a basin was quantified via the coefficient of variation (CV), given as:

$$\mathrm{CV} = \frac{\sigma}{\mu}. \qquad (3)$$

To investigate the regional-scale impacts of the model realisations, the MERIT basins within each region were binned into four elevation bands (following the K1 bands described in Section 10) based on the basin outlet elevation. The mean SWE across all basins within an elevation band within the region was computed. To assess

snow processes on glaciers, the Randolph Glacier Index version 6 (Li et al., 2021) was used. Each glacier shape with a unique GLIMSID was extracted within the broad regions described above. Then, the glaciers were assigned a K1 elevation band and the minimum glacier elevation was used to bin the glaciers, as was done with the MERIT basins. Lastly, the region-wide mean SWE curves were compared between model realisations to compute the difference in melt out date (SWE < 1 mm) between the two model realisations, given as

$$\Delta\text{melt out date} = \text{simulated SWE with redistribution} - \text{simulated SWE without redistribtion.} \quad (4)$$

11 Results

11.1 Snow-Covered Area

Two model realisations, with and without redistribution (blowing snow and avalanches along with associated sublimation), were compared to the LS8 and S2 optical SCA, shown in Figure 10 at a daily temporal resolution as black and dotted-red, respectively. Because each satellite pass did not cover the entire simulation domain at once, this timeseries represents essentially a random sample of the domain at some moment. Therefore, the fluctuations in low to high SCA values are not indicative of snowfall–melt cycles. Rather, they are indicative of sampling different sub-areas of the simulation domain that had different snow covers. Because SCA observations are a random sampling of the simulation domain in time, the analysis is dominated by the large open areas.

The error metrics — MB ($model - obs$), RMSE, and r^2 — between each model realisation and the observed SCA are summarized in Table 1 for the entire water year (October–October) and three seasons: winter (October–March), spring (April–June), and summer (July–August). Throughout the entire simulation period, the with-redistribution realisation had the lowest MB, the lowest RMSE, and the highest r^2 of 0.10, -0.01, and 0.89 respectively. The largest improvement occurred during the summer, where SCA agreement was much improved with-redistribution versus the without-redistribution realisation (r^2=0.91 vs. r^2=0.71, respectively). This improvement was due to simulation of late-lying drifts that slowly ablated.

11.2 Optical Comparison

A qualitative comparison of the optical imagery of April 6, 2021 from Sentinel-2 and the two model realisations with and without redistribution is shown in Figure 11. The comparison allows for visually diagnosing the differences from including the redistribution processes. The illustrated area is $\approx$ 15 km east of the Fortress Mountain Research Basin and was selected due to having substantial contrasting slopes of erosion and deposition. In this figure, the observed optical imagery is shown in the top left. In the top right and bottom right panes are the simulated SWE overlain on the DEM. Areas with 0 mm SWE have no colour associated. Lastly, although there are areas with more than 500 mm SWE, the values were clipped to this for illustrative purposes. In all panes, the tree line is shown in a green line.

The optical image shows a wind exposed alpine-subalpine area, known for large avalanches, in the eastern Rockies that produces a spatially variable snowpack. The windward above-treeline dark areas in the optical imager are these windswept locations, while the white areas are snow cover. In the with-redistribution pane (top right), these windswept locations are clearly visible as dark areas without colour, whereas the snow cover is dark blue. In contrast, the without-redistribution realisation completely failed to capture these regions and produced a generally homogeneous SWE across the domain. The simulation with redistribution simulates little accumulation on the windward slopes, whereas some snow can be seen on the windward slopes in the observations.

11.3 Fortress Mountain Lidar

The spatial comparison of the UAS-lidar snow depth observation, resampled and grid aligned to match the model output, and the two model realisations are shown in Figure 12. The MB, RMSE, and CV are summarized in Table 2, and this table includes the CV from the lidar observations. The lidar observations included deep avalanche deposits from the main headwall in the southwest portion of the domain. The UAS flights were limited by how close they could fly to the headwall, due to maximum altitude limitations; thus the full extent of the avalanche deposits was missed. The north portion of the lidar domain includes a relatively gentle ridge that, due to a wind flow direction reversal, was typically windswept, producing large leeward (south-side) deposits along the treeline and in the small gullies.

The without-redistribution model realisation failed to capture any of the depth heterogeneity present in the observations throughout the observation domain. The avalanche deposits along the main south headwall were completely missed without-redistribution. In all model realisations, the northern ridge had some heterogeneity from snow surface sublimation loss, but was otherwise missing this ridge's snow mass redistribution. The with-redistribution model realisation captured the south face's avalanche deposits. However, this realisation failed to capture the snow mass redistribution on the lee side and had an increased snowdepth on the north side of this ridge, not the south as was observed. Estimated mean windspeeds over this northern ridge (not shown) indicated that neither the main synoptic windflow of HRDPS nor the windflow downscaling captured the flow reversal that is observed in this area. Lastly, the vegetation dataset showed vegetation on the northern side of this ridge, that disturbed the fetch calculation and limited the initiation of blowing snow.

Overall, there was an underestimation in simulated snow depth throughout the domain of ≈1.4 m for the FSM realisations. *In situ* observations at Fortress have noted significant preferential precipitation deposition on the lee of the headwall (middle of lidar domain) that is not accounted for in HRDPS (due to resolution) or in CHM and was a likely source of this underestimation. The CV of the lidar-derived snowdepth was 0.45. The with-redistribution model realisation overestimated the CV (0.61) whereas the without-redistribution realisations underestimated the CV(0.35).

11.4 Point observations

The comparison of point observations to an area model element is difficult due to the scale mismatch between the two. Because most of the CanSWE and SNOTEL stations correspond to sheltered-site observations in clearings, the model element erroneously classified some small clearings as vegetated. It was found that the impact of redistribution on the model performance was generally limited with almost no difference between the model realisation except at four sites due to the location of the sites being in sheltered locations where little to no snow redistribution occurs. Therefore, the comparison of the model realisations to the observation dataset is shown for the non-redistribution case. The CDFs of MB and RMSE error metrics (denoted by line type) within each region (denoted by line colour) are shown in Figure 13. The mean error values for each region are summarized in each figure subplot.

The majority of the largest underestimation errors was due to the model missing the small sheltered clearings and treating these locations as forested, thereby intercepting a substantial fraction of snowfall. This is shown by the large negative mean bias values. Further, there was a west-to-east decrease in both MB and RMSE errors. There was a 116% reduction in MB and an almost 71% reduction in mean RMSE from Coastal CAN to the Rockies CAN region, with a similar reduction from the Coastal US to the Rockies US. The large standard deviation in errors was reduced from Coastal to the Rockies, as shown in Figure 13. In Coastal CAN and US, there were consistent and systematic failures in predictions versus smaller periodic errors in the Rockies. This systematic error is diagnosed as a large positive precipitation bias in the western part of the domain that decreased towards the east.

At the sheltered point scale, there is no clear advantage of including redistribution. The results between the two realisations are either identical or only slightly perturbed by including redistribution. However, there were four sites where the inclusion of redistribution degraded the point estimation. The worst occurred at a location (BCE-3A28P) where there was an over estimation of blowing snow redistribution that resulted in a small drift at the station. The second location (BCE-3A22P) was on the edge of an avalanche deposit that resulted in an over estimation of SWE. At the third location (ALE-05DD804P), the station is on the edge of a medium-sized clearing, resulting in the model over estimating redistribution to this site. Lastly, the fourth site (BCE-3B17P) is on a mid-elevation slope, and the avalanche routine estimated snow redistribution away from this location, resulting in an under estimation of SWE.

11.5 Coefficient of variation

The CV for each MERIT basin was computed for each model realisation for April 1, 2021, as well as the difference in mean CV between the two realisations (with redistribution - without redistribution), is shown in Figure 14. The CV value was computed across all scales and landforms within the basin, including vegetation. The summary of these CV values for each region (see Figure 1) are summarized in Table 3.

The model realisation with transport (left figure) had higher mean CV values throughout the simulation domain versus the model realisations without (right figure). Because the CV value is the ratio of the standard deviation to the mean, basins that contained large variability between no or shallow snow covers and deep drifts had the highest

CV values. Without-redistribution, there were no deep drifts and few completely eroded slopes (apart from a few areas due to high sublimation loss). A low CV is expected in highly vegetated basins. Therefore, these simulations had a broadly more homogeneous snow cover with variability driven by elevation gradients or significant slope shadowing. This homogeneous snow cover (low CV) is considered a more uniform white shading in the figure for the no-redistribution realisations – low CV of ≈ 0.1 to 0.3. When including redistribution, the variability increased significantly due to blowing snow moving snow from the windward side of the ridges to the leeward side and subsequently being redistributed to a lower elevation via avalanches. The difference in CV between the two model realisations is shown on the bottom row and highlights the locations where the over-winter snow redistribution was most active.

Owing to a large amount of precipitation in the Canadian Coastal region, all realisations had substantial April 1 SWE amounts. Therefore, the CV was less dominated by zero values and had CV values of 1.2 (with-redistribution) and 1.1 (no redistribution). In the US coastal region, the CV increased to 2.6 (with-redistribution) due to the sparser low elevation snow covers. Throughout the Interior CAN domain, the CV was low due to shallower and more spatially sparse snowpacks (lower SCA). The Interior US, in contrast, had an exceptionally high CV, likely due to FSM ablating thin and shallow snowpacks, thus producing a large standard deviation and low mean. The CV then increased towards the Canadian Rockies due to a mix of eroded slopes and deep snowpacks deposits in drifts and avalanche runs, such as those shown in Figure 11.

11.6 Regional-scale impacts

The mean SWE across all MERIT basins, within an elevation band within a region, was computed and is shown in for the period April 1, 2021 onward in Figure 15. The results from the with-redistribution realisation are shown in red and without-redistribution realisation in dashed-black. There are regional and elevation patterns to the impact of including redistribution on the SWE accumulation and ablation curves, as shown in Figure 15. Except Coastal CAN at high elevation, the inclusion of redistribution processes resulted in an areal snowpack that fully ablated later in the season in all regions and elevation bands. The impact of the model realisation on the melt out date is evident in the figure. The regions with the largest differences between realisations were often regions with glaciers, such as the Coastal CAN region. Much of the mid- and high-elevation bands in the other regions also contained glaciers. In contrast to the Coastal CAN region, some regions such as the Interior US 1500 m–2500 m band did not show much mean SWE difference between with- and without-redistribution realisations.

In the high-snowfall region of the Coastal CAN and US, both realisations predicted snowpacks to persist into late summer and perennial snowpacks into the next season. However, these two regions had the largest difference in the impact on SWE depletion curves from the two model realisations. Due to the model realisations predicting some perennial snowpacks in many basins, the mean SWE curve did not ever fulfill the criteria for “no snow”, and thus the difference between the model realisations is 0 days. In the Coastal CAN region in the 1500m - 2500m elevation band, the inclusion of redistribution had an impact starting in early winter (Dec) that led to a lower peak SWE than without-redistribution at the high elevation. The lower peak SWE was due to the loss from blowing snow sublimation and redistribution of snow from high elevations to lower elevations — both within this elevation band and into other elevation bands. Across all regions, this mass redistribution process was a dynamic, cascading process. Throughout the rest of the regions, the difference in ablation ranged between 2 days and 87 days, with a mean of 33.75 days. The error introduced by not incorporating redistribution processes in aggregate for each of the regions resulted in steadily increasing in error throughout the ablation season. As a result, errors of up to 100% at the regional scale in the absence of redistribution processes were possible, stemming from missing the late-lying snow deposits. These errors are more pronounced in the drier, non-coastal areas that are more sensitive due to relatively shallower snowpacks and a lack of perennial snowpacks. These errors lasted up to a couple of months, likely impacting the local hydrology and ecosystems.

12 Discussion

The observed intra-annual heterogeneity introduced by incorporating redistribution physics on snow covers is clear (e.g., Pomeroy et al. (1993); MacDonald et al. (2009); Mott et al. (2010); Mott et al. (2018); Marsh et al. (2020a); Vionnet et al. (2021b)). However, the incorporation of redistribution in a spatially distributed model has not previously been shown over large spatial extents at snowdrift-permitting scales. In Vionnet et al. (2021b), evaluation of snow redistribution was done using airborne lidar. However, such data do not exist across the ≈ 1.4 M km^2 extent investigated here. Nor do any data exist such as Pléiades-derived snow depths. Wayand et al. (2018) proposed a

snow-persistence and absence index, derived from Landsat and Sentinel optical images, that is an accumulation of the number of days with or without snow. Because of the spatially and temporally sparse satellite observations due to repeat frequency, cloud cover, and the size of the domain, there were insufficient per-pixel observations for the year. Further, it only provides an estimate of how many days during a period that snow was present or absent. Thus, a perfect score may be obtained when the model predicts snow present in the first 15 days while observation have snow in the last 15 days. Therefore, this work relied upon an optically derived SCA analysis. Using remote sensed SCA to diagnose the model is difficult owing to the spatially and temporal sparse observations due to repeat frequency, cloud cover, and the size of the domain. Gap-filling techniques for the SCA observations are possible, e.g., Gascoin et al. (2015); however, there is likely significant uncertainty when infilling SCA in a region of millions of km^2. The inability to diagnose sub-canopy snow coverage is a major limitation of the SCA technique due to the significant evergreen canopy coverage in the simulation domain (Figure 6). In the optical images and field observations, small topographic features such as gullies and surface roughness from rocks and scrub vegetation hold small amounts of snow. However, the numerical model does not include these sub-grid features. A major limitation is in the mid-winter observations of redistribution due to the cross-ridge length scale being approximately that of a few satellite pixels. Thus, a small subset of the evaluation dataset is where most of the redistribution process occurred during winter months. Observation of these small features is further exacerbated due to mid-winter high-elevation cloud covers. Late-season SCA estimates from observations were better, due to large late-lying avalanche deposits and more clear days. Despite these limitations, late-season improvements in simulated SCA were clearly seen by including redistribution processes.

The lidar UAS data provided a unique evaluation dataset by providing the only sub-canopy snow depth evaluation and providing a high-resolution comparison to CHM. The spatial locations of the simulated avalanche deposits were well predicted and demonstrated the impact of redistributing high elevation snow to lower elevations. Unfortunately, the north side of the north ridge in the Fortress domain was parametrized as forested, limiting blowing snow generation. The wind flow reversal that is observed in this area was also not well captured. Without manually correcting in this area (and the time-consuming correction throughout the entire domain) it is not possible to resolve this. Future work should examine whether the newer vegetation products have better representations of forest clearings and treelines, and whether a continued effort on wind downscaling must be made to better capture these fine-scale windflow behaviours.

As noted by Horton and Haegeli (2022), there is a substantial precipitation bias in HRDPS in the western coastal portion of the domain and NWP systems face numerous challenges in Western Canada, e.g., Mo et al. (2019). Certainly, the observation network is sparse, and thus the NWP outputs are the only range-wide estimates available. However, when compared to the on-the-ground SWE observations of CanSWE, the simulated SWE is dramatically overestimated in the coastal region. This regional bias persisted in simulations with and without redistribution, thus eliminating incorrect redistribution as a cause. Despite this, NWP outputs remain an optimal choice because the current version of the precipitation analysis products in this region have few surface observations to use and do not typically perform better due to limitations in the spatial interpolation algorithms that do not consider the effect of topography (Schirmer and Jamieson, 2015; Fortin et al., 2018). CHM has been extensively tested in the Canadian Rockies using a small subset of the HRDPS domain (e.g., Vionnet et al. (2021b)), and thus this bias had not been previously observed. Models such as CHM can provide short-term forecasts using HRDPS, and therefore using these predictive models for forecasts motivates developing methods that are robust to these biases. Herein, using a forecast product is of interest because of the ability to forecast with it. Long-term work should continue to support high-resolution operational re-analysis products to help alleviate these biases because local, bespoke corrections are not robust.

At a MERIT basin scale and at the regional scale, the impact of neglecting redistribution is clear, with percent difference errors of 100% persisting for one or two months. This corresponds to fully ablating a basin's snowpack, versus persisting drifts into late summer. Avalanches moving snow to glaciers is a key source of glacier preservation under climate change. The sensitivity to not including redistribution was increased in the drier areas of the domain and lower elevations. Because future climate change scenarios suggest an increased occurrence of mid-winter melts (e.g., Musselman et al. (2017)) and a reduction in snow redistribution (Rasouli et al., 2022; Fang and Pomeroy, 2023), including redistribution processes will better estimate summer snowpacks in a warmer world. Without redistribution, estimates may predict premature ablation. Thus, the hydrological and glaciological relevance is clear; future work should quantify the impacts on estimated hydrographs and glacier mass balance and how redistribution processes may change under future climate change scenarios.

13 Conclusions

Snow redistribution via blowing snow and avalanches, sublimation, and mid-winter melts are the primary processes that shape the areal distribution of snowpacks in mountain regions throughout the winter. The wind transports snow from the wind exposed to sheltered sites, creating cornices and accumulation on leeward slopes that then avalanche downslope, resulting in deep snowdrifts and deposits that persist into summer. Snow redistribution can also be critical in transporting snow onto glaciers. However, including such redistribution processes in spatially explicit models is computationally expensive, and thus they have been typically excluded.

In this work, CHM was used to evaluate the possibility of simulating snow redistribution and sublimation processes over 1.37M km^2 and quantify the impact on ablation curves of neglecting these processes on simulating late-lying snow covers. CHM used a variable-resolution, unstructured representation of the Earth's surface to reduce the number of computational elements by 98.9% compared to the original rasters while maintaining a minimum 50-m length scale in areas of complex heterogeneity, such as ridge lines. Improvements in CHM's high-performance computing usage to utilize distributed computing and the introduction of a massively parallel numerical solver allowed for large-extent application.

Clear improvements in snowpack heterogeneity have been previously shown at small scales; however, the large regional impacts were unclear. Here, redistribution and sublimation processes have been shown to be important at basin and regional scales. Simulations of summer SCA compared to satellite observations were greatly improved by including snow redistribution and sublimation. At the regional scale, the inclusion of snow redistribution and sublimation resulted in delaying full snowpack ablation by 33 days on average. In some regions, errors of 100% for multiple months were possible when snow redistribution was excluded, corresponding to fully ablating a basin's snowpack, versus persisting drifts into late summer. The persistence of snow with the redistribution realisations and the lower peak SWE at high elevations was due to the erosion of snow by the redistribution mechanisms at a high elevation and transport to lower elevations. This sensitivity was increased in the drier areas of the domain and at lower elevations. This work is the first explicitly distributed simulation of these processes at such a large spatial extent and demonstrates that including these processes is critical for estimating snowpack dynamics and representing snow water resources in mountain headwaters.

14 Acknowledgements

The authors would like to acknowledge funding support from the Canada First Research Excellence Fund's Global Water Futures programme, NSERC Discovery Grants, Alberta Innovates and the Canada Research Chair programme. Logistical support for UAS was provided by Fortress Mountain Resort and snow surveys by Kieran Lehan, Greg Galloway, and Robin Heavens of the Centre for Hydrology in Canmore, Alberta. This paper is a contribution to the UN International Year for Glaciers' Preservation-2025. The authors would like to thank Dr. Kevin Green for his assistance developing the MPI component of CHM.

15 Open Research

The open-source CHM model code (Marsh et al. (2020b), https://doi.org/10.5194/gmd-13-225-2020) is available at https://github.com/Chrismarsh/CHM. The Mesher algorithm (Marsh et al. (2018), https://doi.org/10.1016/j.cageo.2018.06.009) is available at https://github.com/Chrismarsh/mesher. The high-resolution wind library has been generated using the WindNinja diagnostic wind model (Forthofer et al. (2014), https://doi.org/10.1071/WF12089; https://weather.firelab.org/windninja/), via the Windmapper tool (Marsh et al. (2023b), https://github.com/Chrismarsh/Windmapper, https://doi.org/10.1029/2022WR032683). HRDPS forecasts are distributed on the Canadian Surface Prediction Archive (CaSPAr, https://caspar-data.ca/, Mai et al. (2019), https://doi.org/10.1175/BAMS-D-19-0143.1). The US Snow Telemetry (SNOTEL) data (snow and precipitation) are available at https://www.nrcs.usda.gov/wps/portal/wcc/home/snowClimateMonitoring/ and have been downloaded using the soilDB R package (http://ncss-tech.github.io/AQP/soilDB/soilDB-Intro.html). The CanSWE dataset is available at (Vionnet et al. (2021a), https://zenodo.org/records/7734616). The lidar snow-depth dataset will be made available with a DOI upon publication.

16 Figures

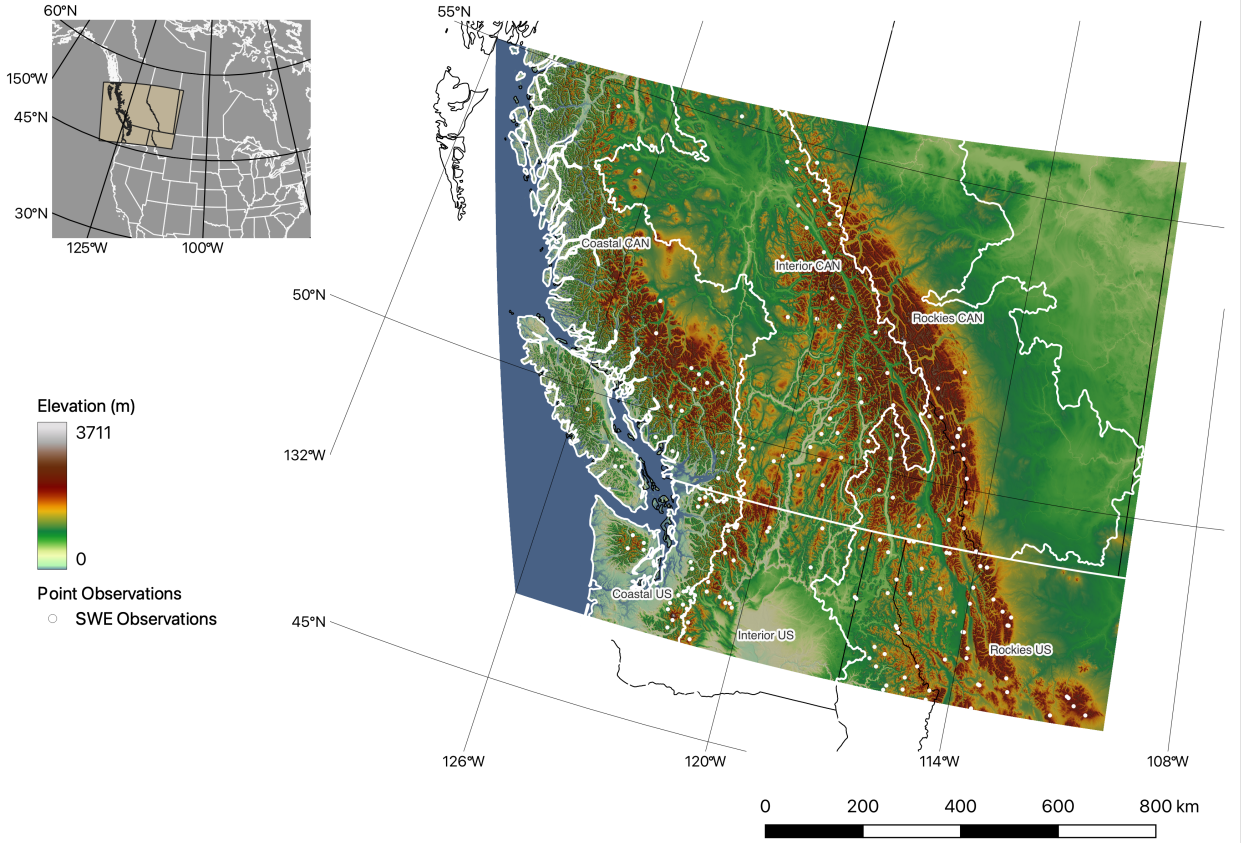

Figure 1: The simulation domain of approximately 1.37M km^2 covering the Western Canadian Cordillera region and some parts of the northern United States. Broad regions are shown in white. Observation stations from the CanSWE and SNOTEL datasets used in the evaluation are shown as white dots.

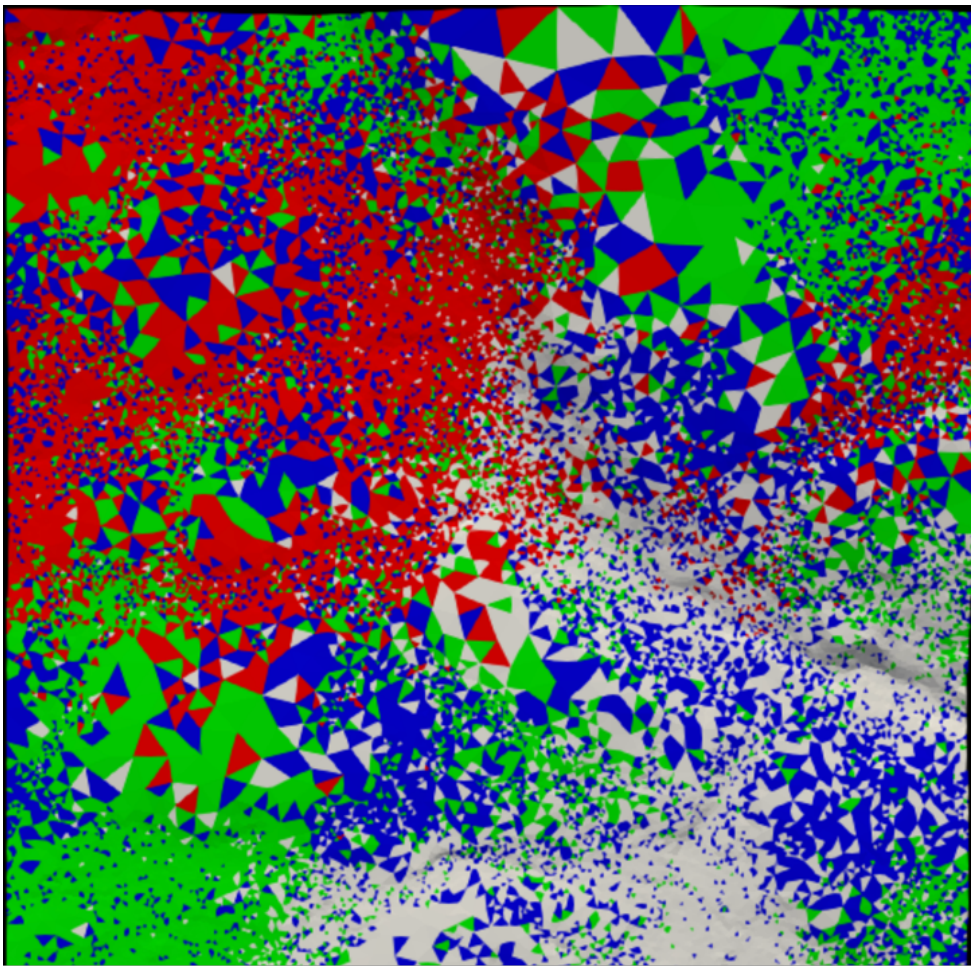

Figure 2: Naive domain decomposition of an unstructured mesh for four MPI ranks. The ranks are coloured as green, blue, red, and white. The unstructured triangle ordering results in poor MPI performance because close in space triangles may not be close in memory and thus may reside on another MPI rank.

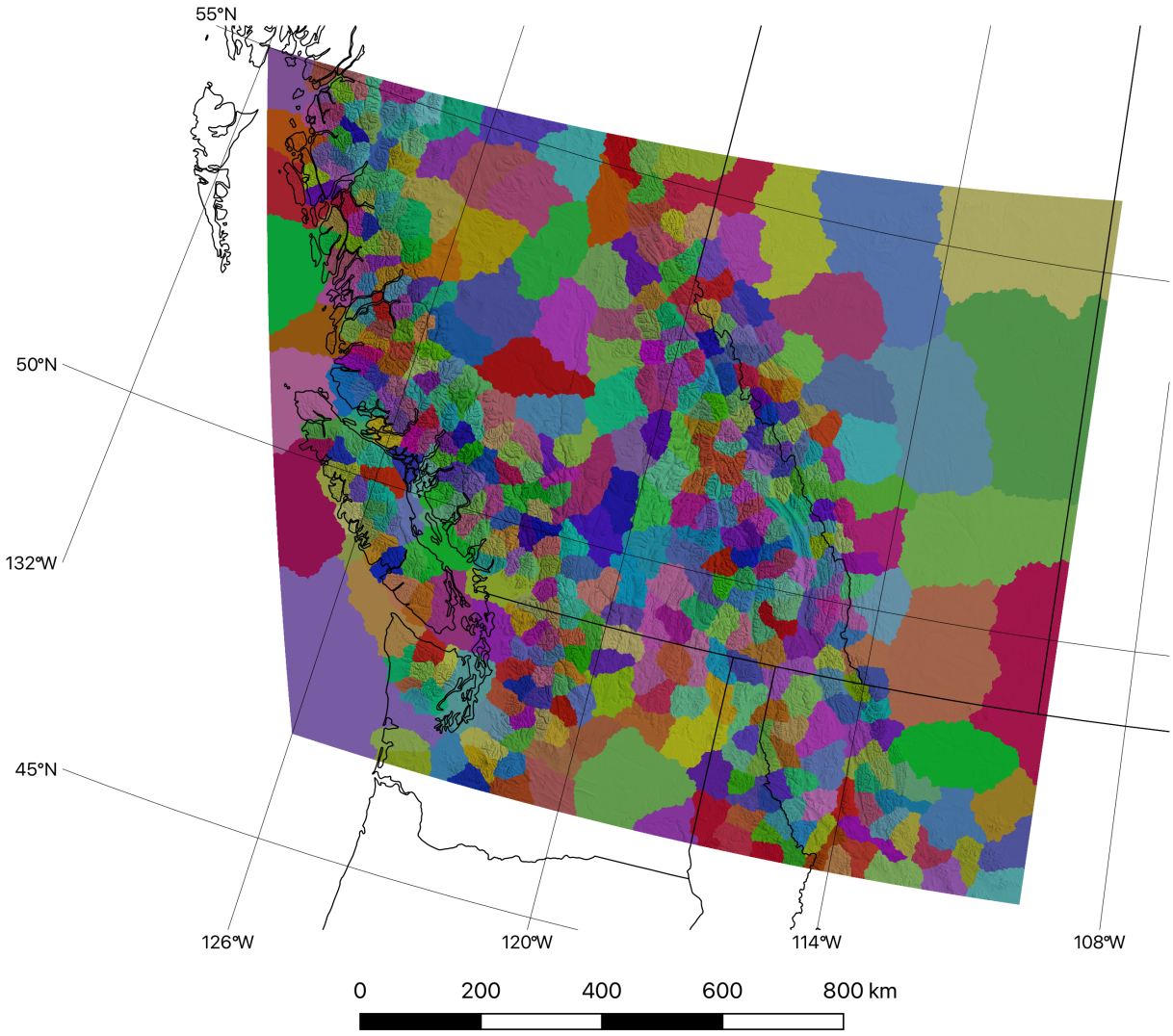

Figure 3: The METIS fill-reducing ordering partition for 448 MPI ranks. Although these partitions may look like hydrological basins, they are not. Each colour denotes an MPI rank (colours are reused).

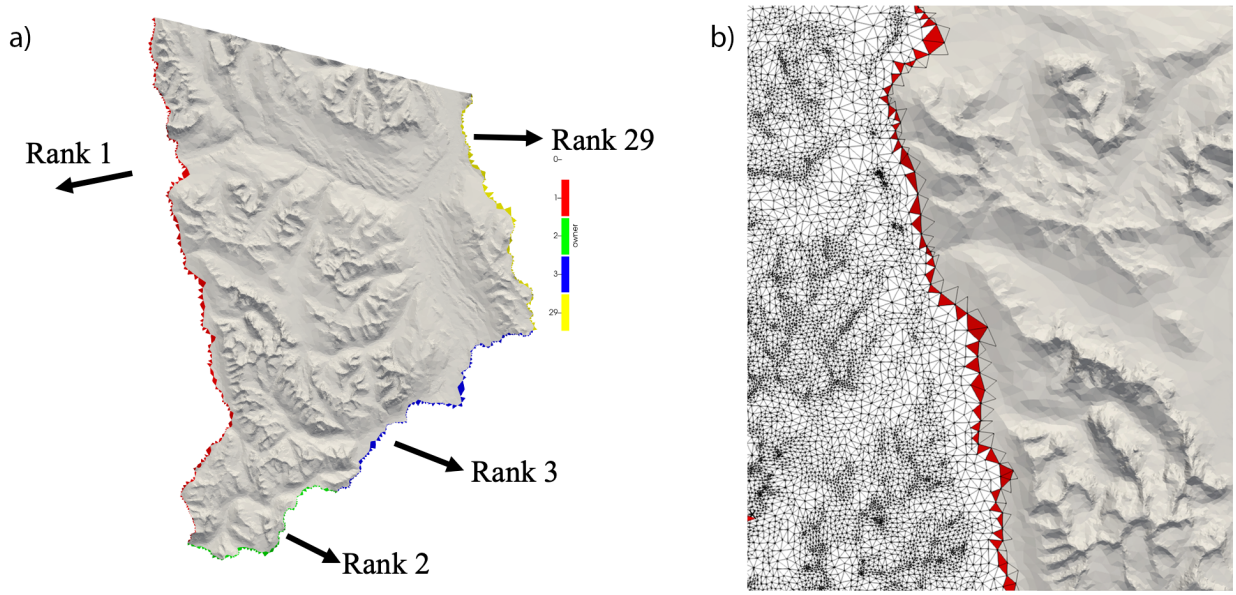

Figure 4: Type I ghosts in: a) colour, showing which ranks they communicate with and a zoomed in region b) showing the overlapping mesh for MPI rank 1 (hollow fill).

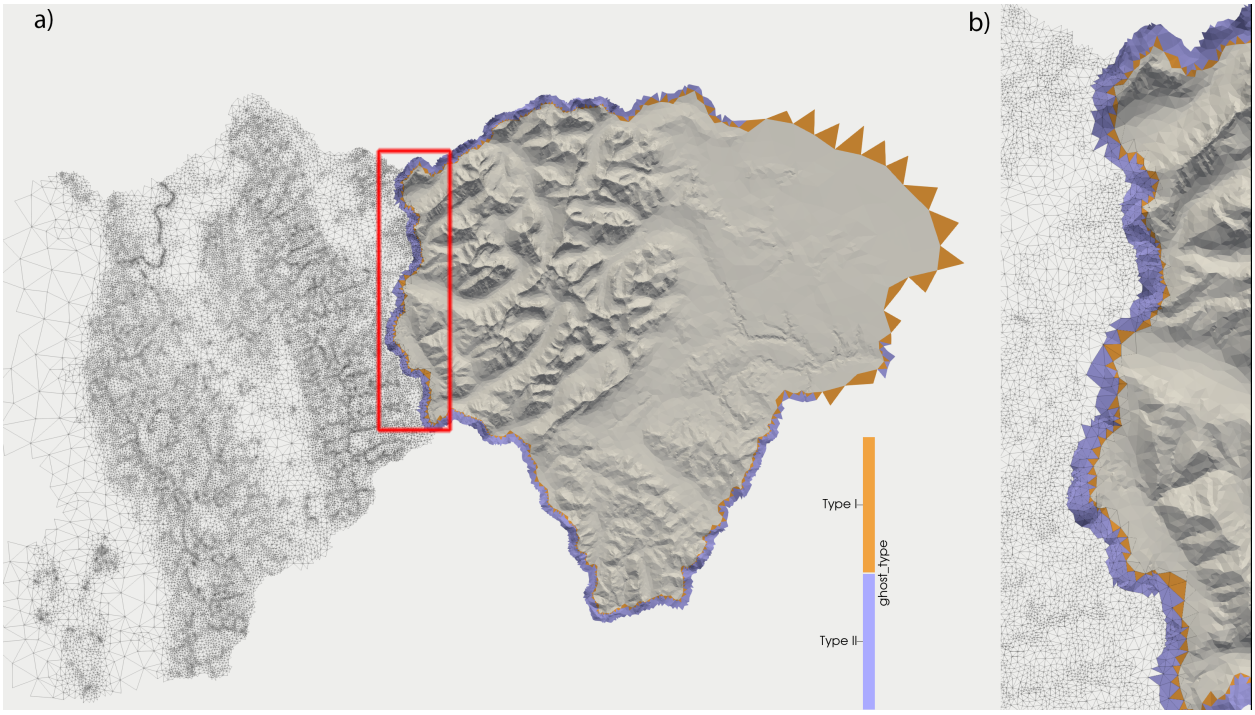

Figure 5: (a) Type I ghosts (orange) and Type II ghosts (purple). Type I ghosts are used in direct MPI communication whereas type II ghosts are only used for landscape queries. (b) shows a zoomed-in section to better illustrate how ghosts allow for partition overlap. In both (a) and (b), the neighbour partition is shown as hollow triangles. No Type II ghosts are present on the far east (right) side of the domain due to the size of the triangles (larger than 1 km).

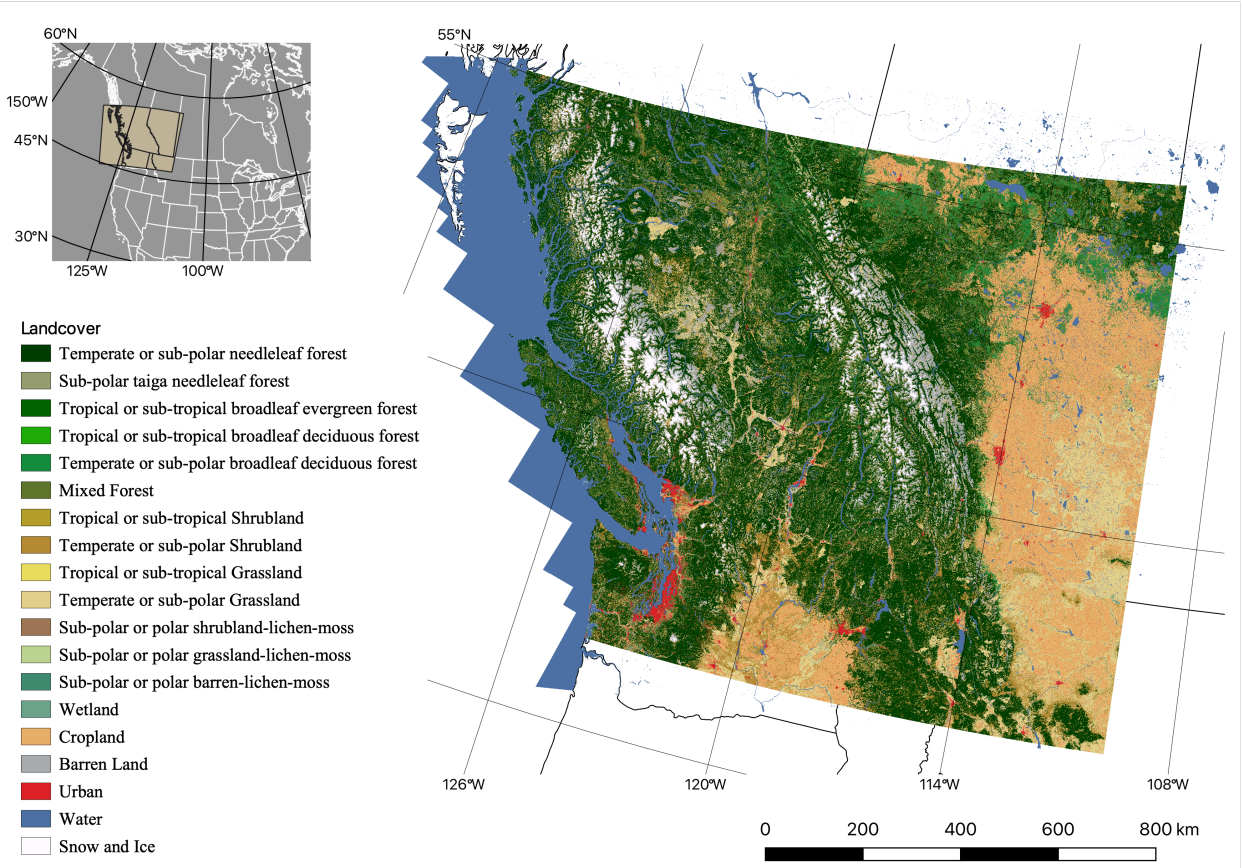

Figure 6: The North American Land Change Monitoring System (NALCMS; Latifovic et al. (2016)) 30 m vegetation classification used. The Hansen et al. (2013) water mask is shown in blue.

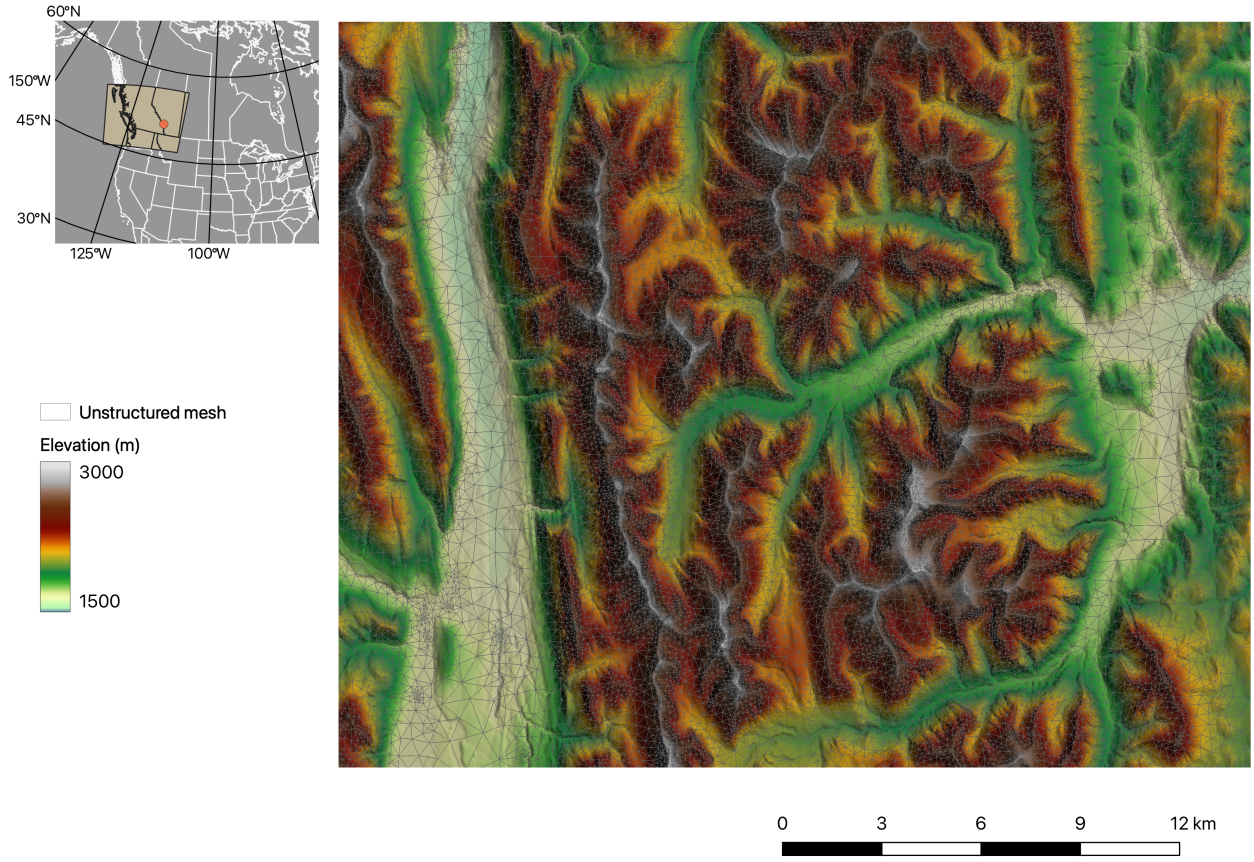

Figure 7: A zoomed-in portion of the simulation domain showing the variable-resolution unstructured triangular mesh in grey overtop of the raster DEM. The variable-resolution mesh had a minimum triangle area of 50 m x 50 m and a maximum vertical error, as measured by Root Mean Squared Error (RMSE) to the source raster DEM, of 15 m.

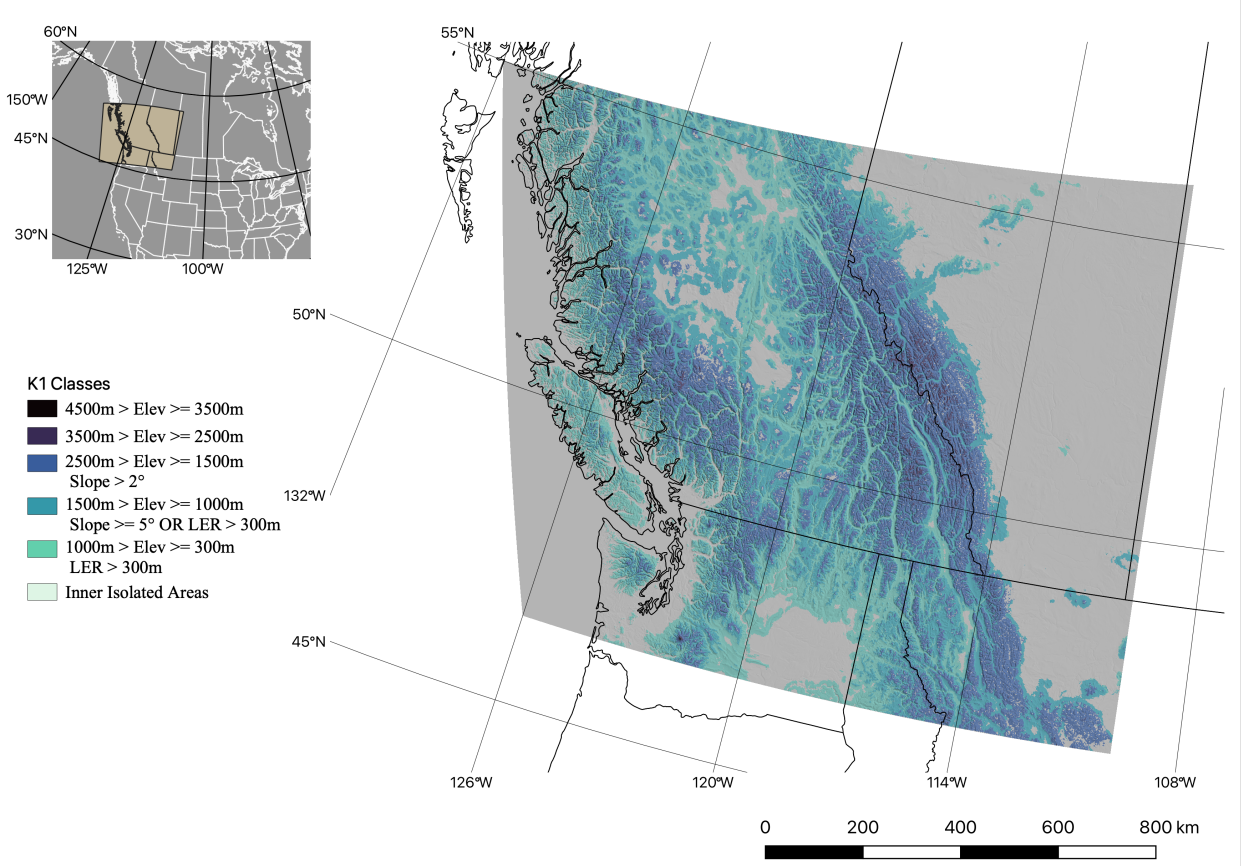

Figure 8: K1 mountain ecozones following Kapos et al. (2000), based on elevation and slope and were at 1 km resolution. The following K1 elevation breaks were used: 0 m, 500 m, 1000 m, 1500 m, 2500 m, and 3500 m.

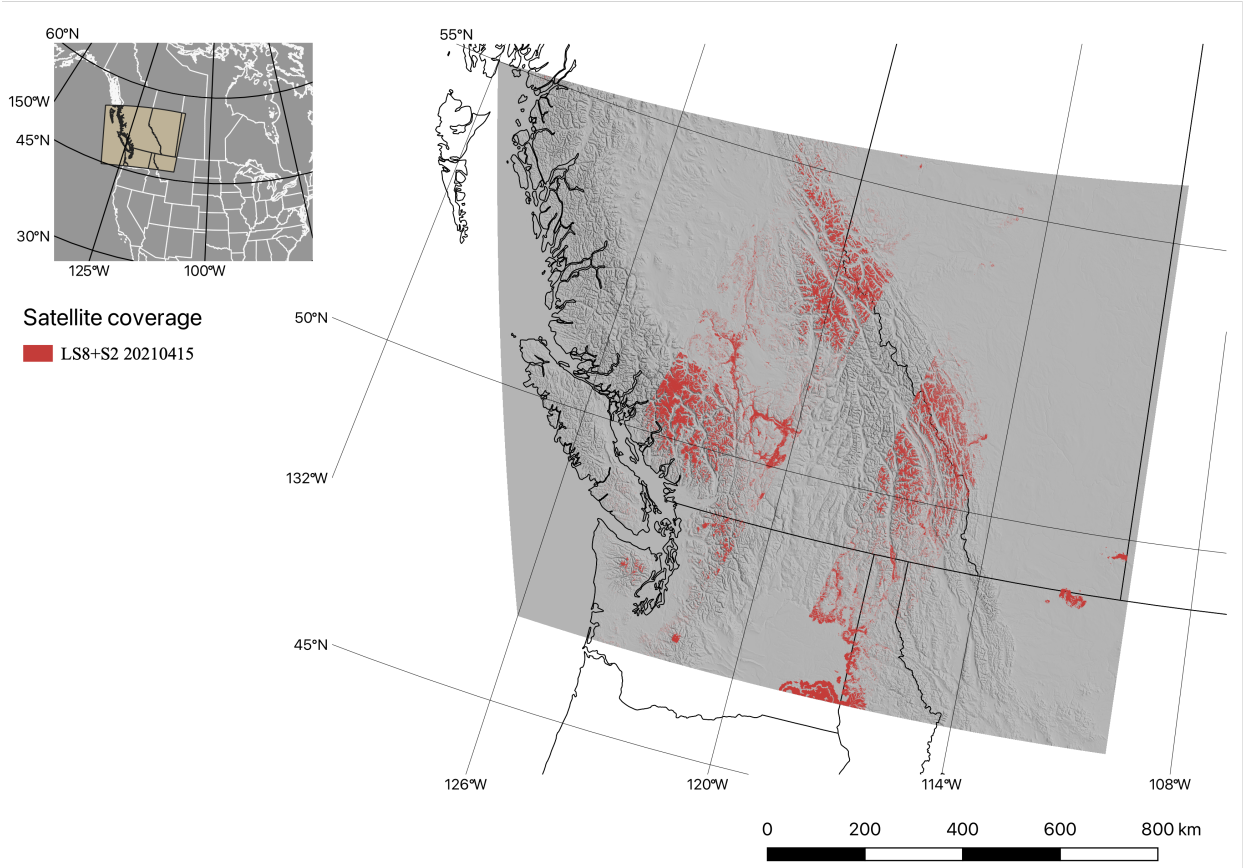

Figure 9: Example of available satellite optical imagery (shown in red) from Landsat 8 (LS8) and Sentinel-2 (S2) after being masked for clouds and vegetation for April 15, 2021.

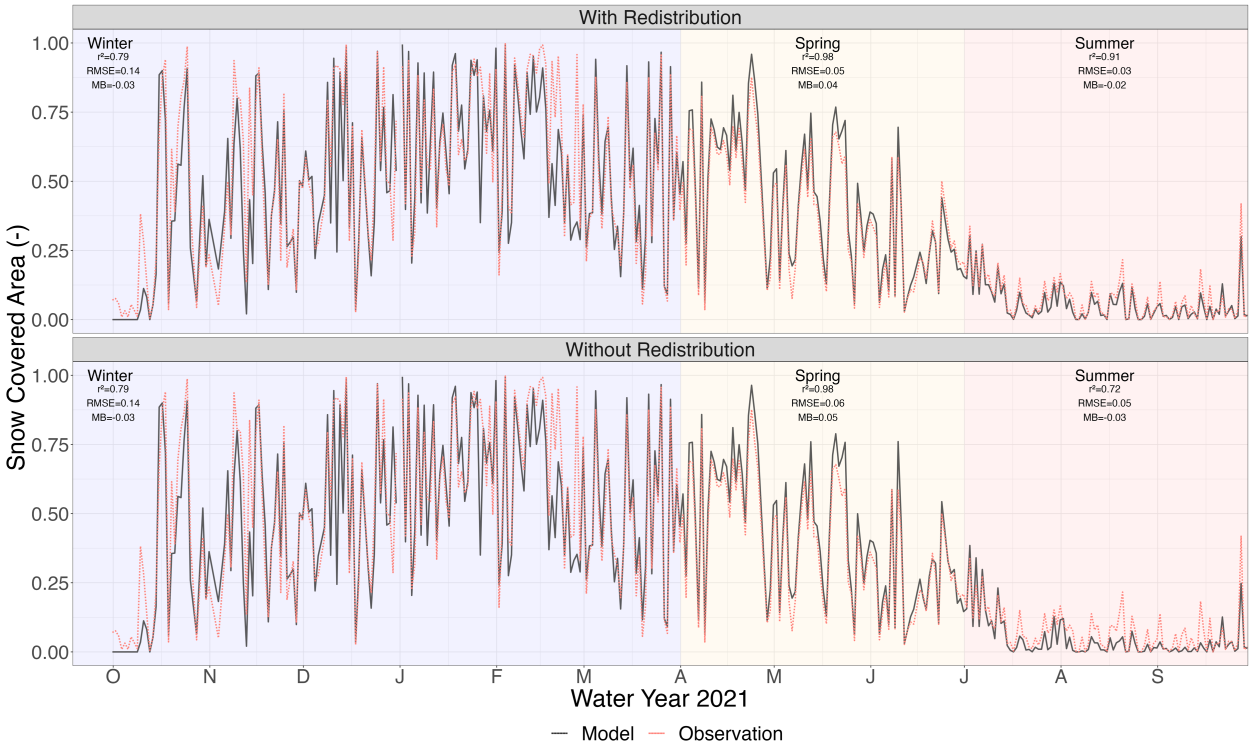

Figure 10: The two model realizations with and without redistribution (blowing snow and avalanching) in black as compared to the combined LandSat 8 and Sentinel-2 optical snow-covered area (-) in dotted-red.

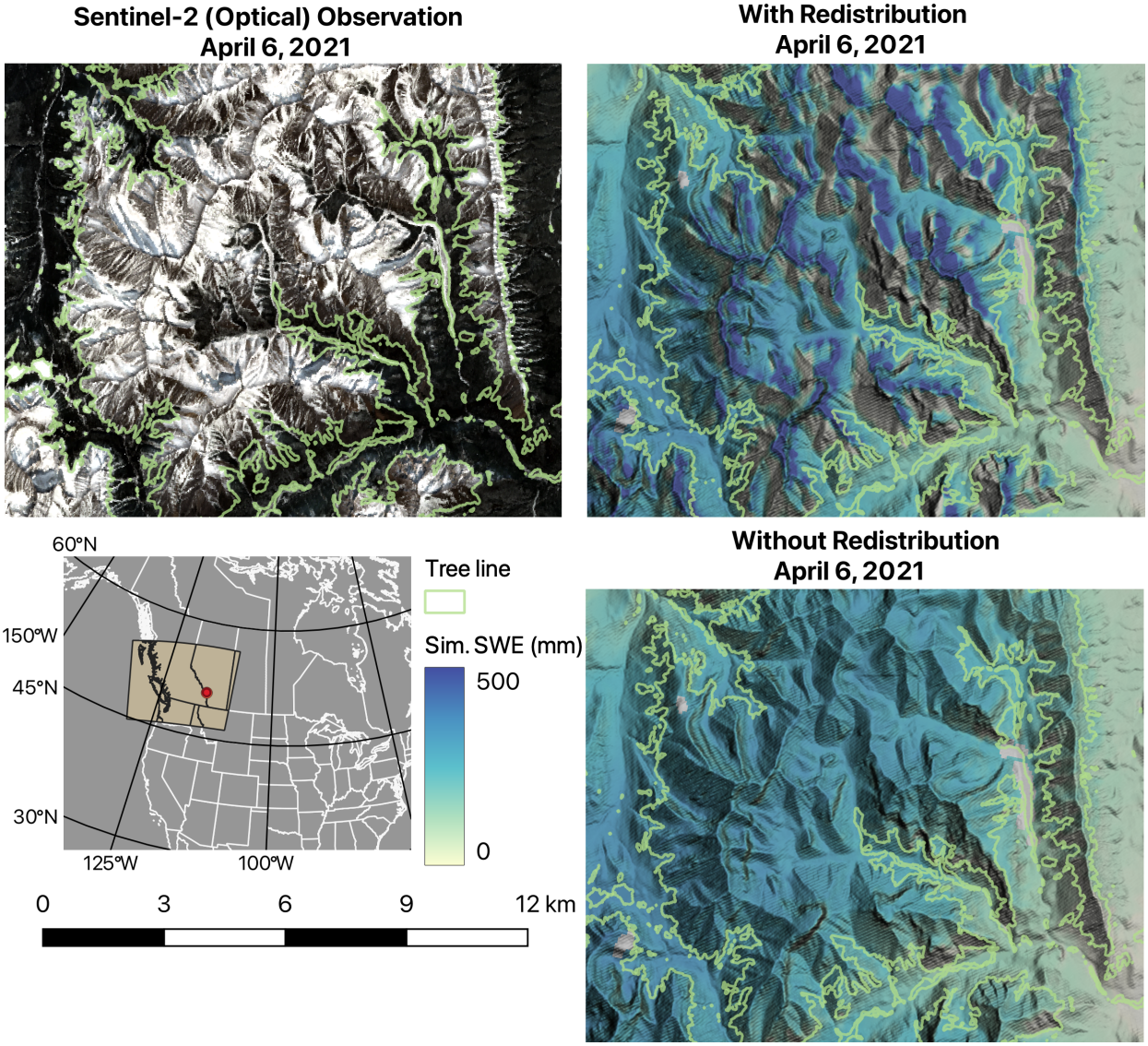

Figure 11: Optical imagery for April 6, 2021 (top left) and simulated SWE for the realisations with-redistribution (blowing snow and avalanches; top right) and without-redistribution (bottom right) 15 km east of Fortress Mountain. This location was chosen due to the mix of various aspects and snow/snow-free locations. The treeline is shown as the green boundary in all sub-figures.

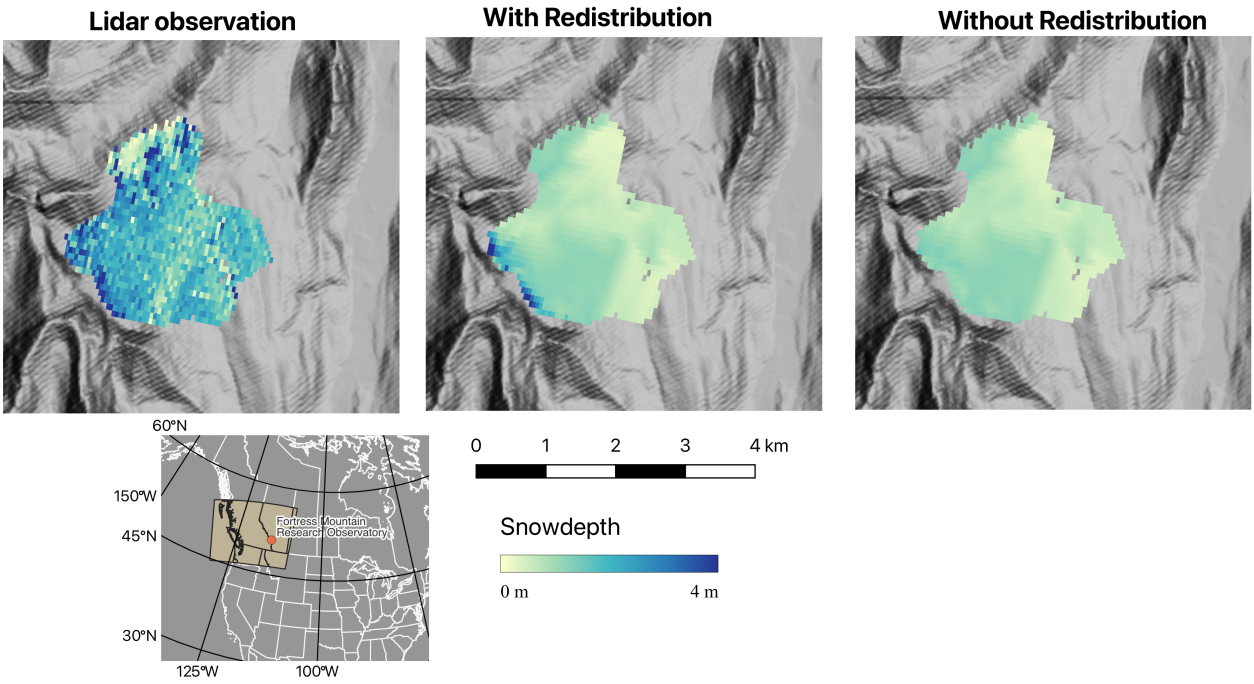

Figure 12: Observed snowdepth from UAS lidar observations (left) along with the two model realisations with- and without-redistribution (blowing snow and avalanching) for May 4, 2021 at the Fortress Mountain Research Basin. The lidar is grid aligned to match the model grid.

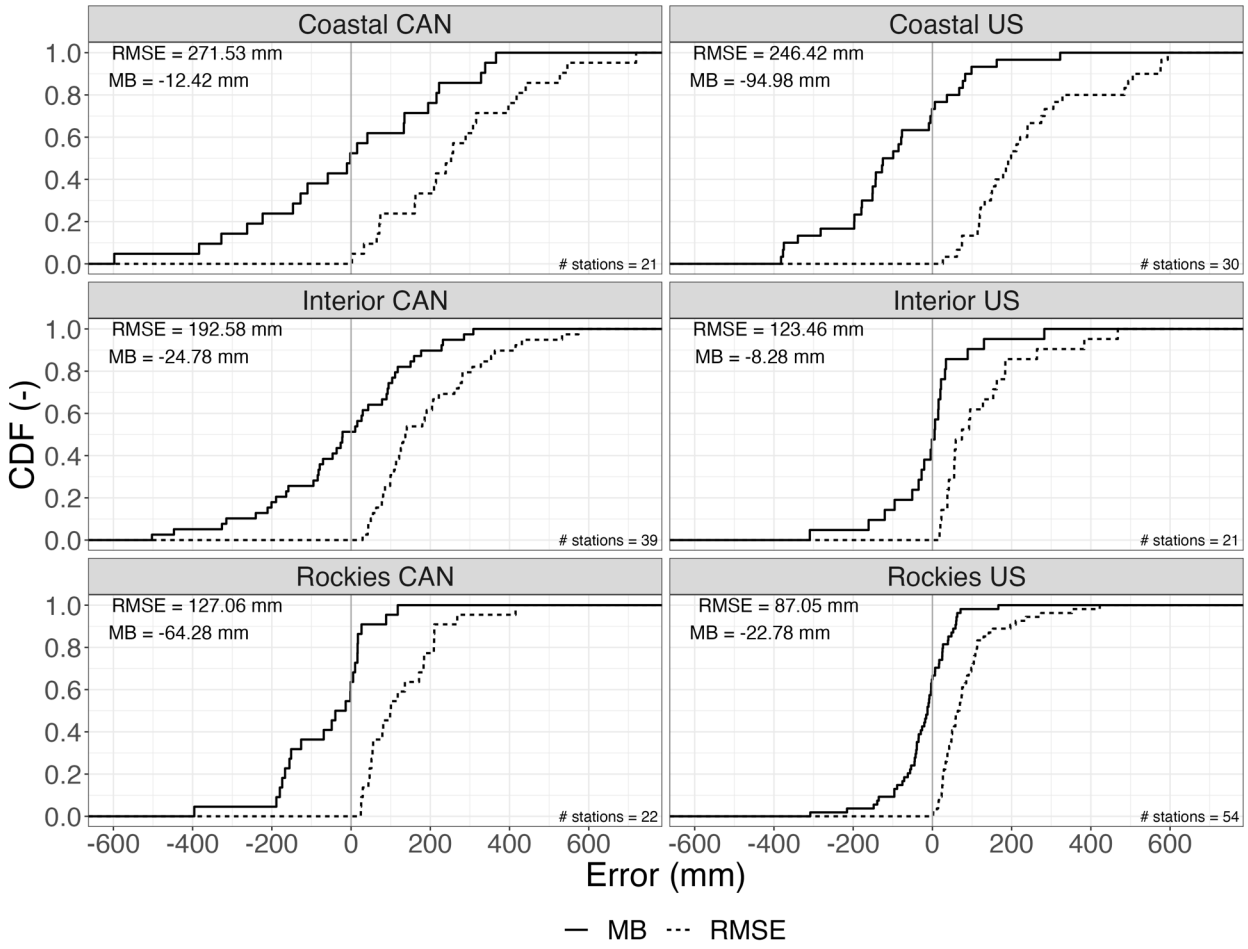

Figure 13: The RMSE (mm; solid line) and MB (mm; dashed line) was computed between the modelled SWE and point observations of SWE from CanSWE and SNOTEL. The CDF of these are plotted for each region. The mean MB and mean RMSE for each region are reported in the top left of each sub figure. The number of observation stations in this region is in the bottom right.

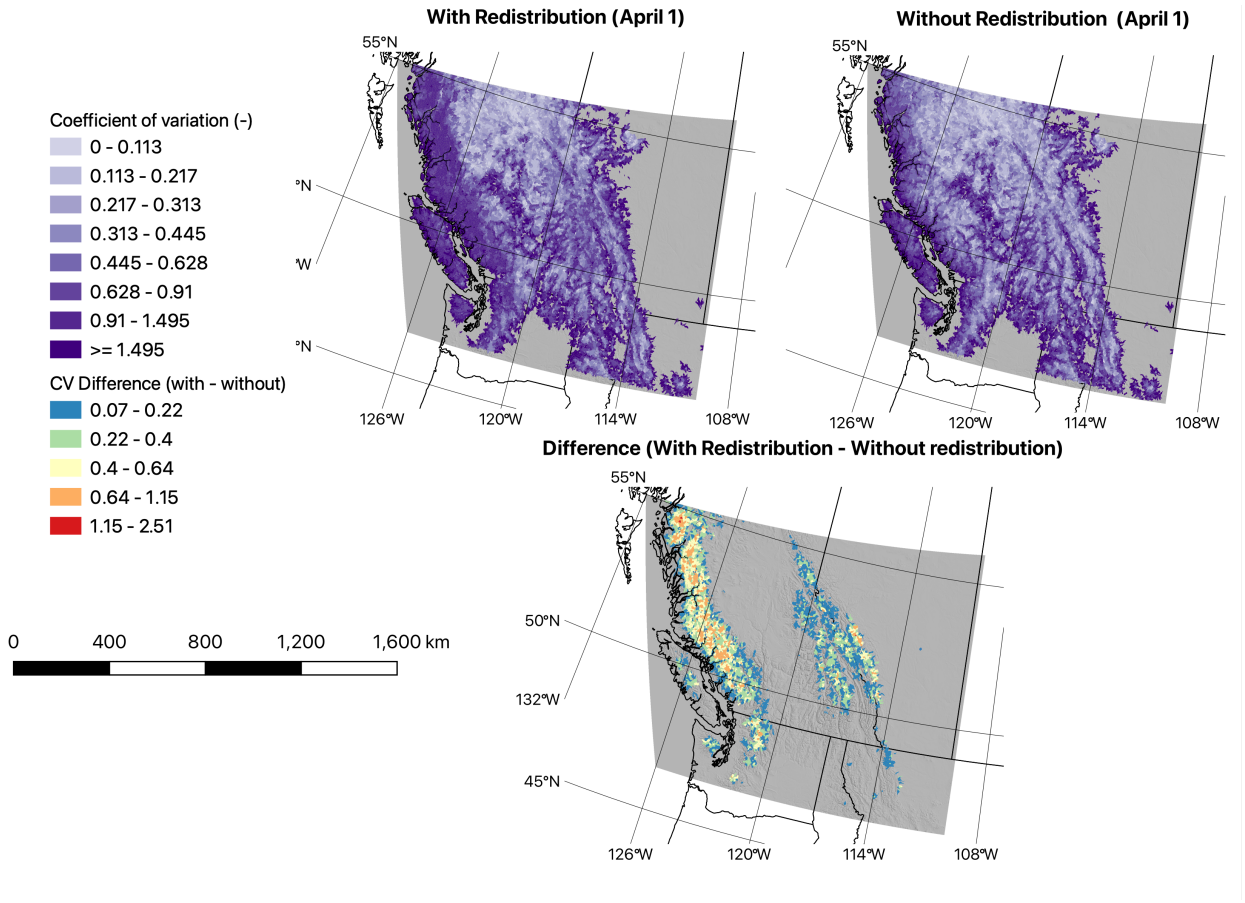

Figure 14: Mean coefficient of variation of simulated SWE for each MERIT basin, for April 1, 2021. Top left: with snow redistribution. Top right: without redistribution. Bottom: difference in CV between model realizations (with redistribution - without redistribution).

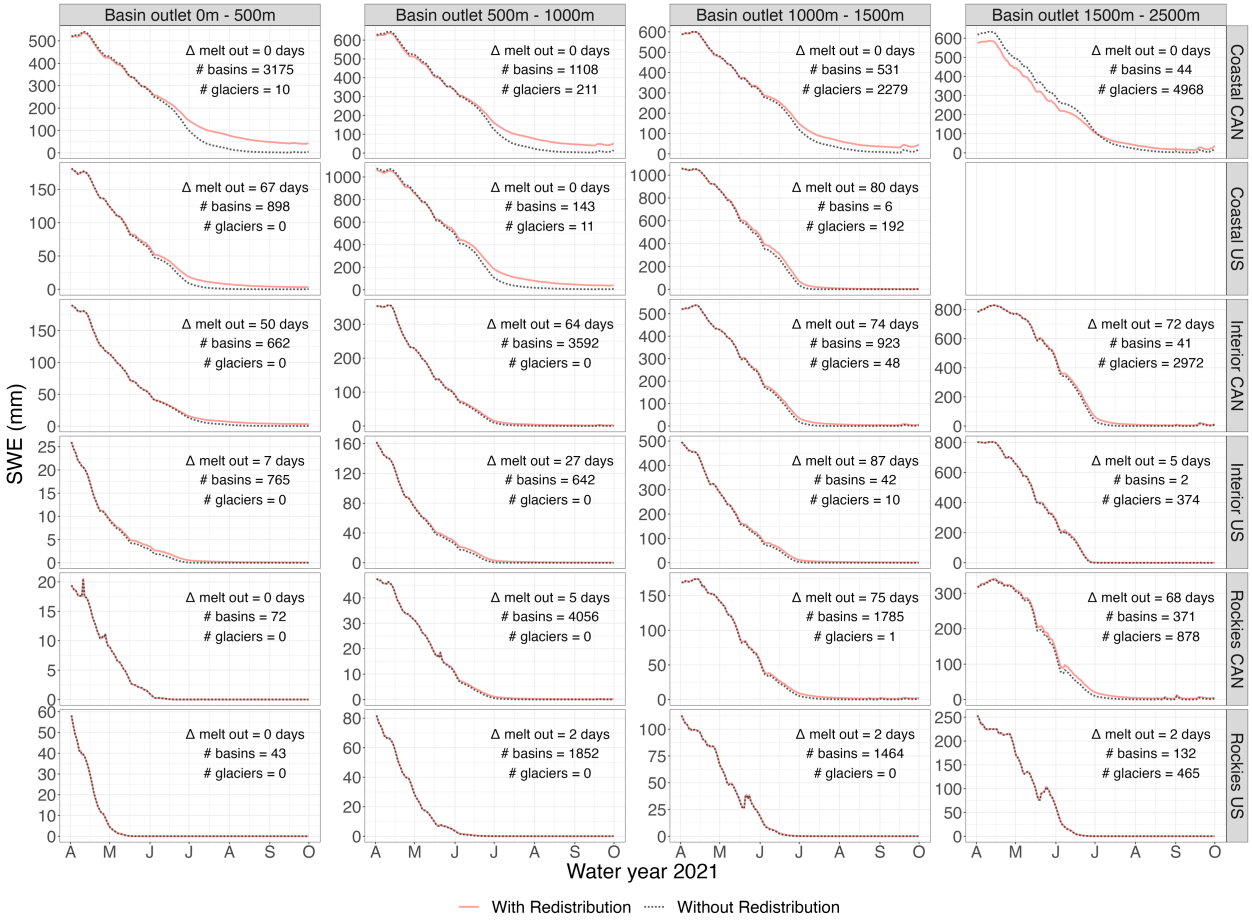

Figure 15: The mean SWE across all MERIT basins within an elevation band within a region was computed for the two model realisations. MERIT basins were binned according to outlet elevation.

17 Tables

Table 1: Root mean squared error (RMSE), r^2, and mean bias (MB; $model - obs$) for observed SCA versus modelled SCA for each model realisation for: the entire water year and winter (October–March), spring (April–June), and summer (July–August).

Season	Realisation	RMSE (-)	r^2	MB (-)
Spring	With Redistribution	0.05	0.98	0.04
Spring	Without Redistribution	0.06	0.98	0.05
Summer	With Redistribution	0.03	0.91	-0.02
Summer	Without Redistribution	0.05	0.72	-0.03
Winter	With Redistribution	0.14	0.79	-0.03
Winter	Without Redistribution	0.14	0.79	-0.03
Water Year	With Redistribution	0.10	0.89	-0.01

Season	Realisation	RMSE (-)	r^2	MB (-)
Water Year	Without Redistribution	0.11	0.88	-0.01

Table 2: Mean bias (MB; $Simulated - Obs$), root mean squared error (RMSE), and coefficient of variation (CV) for observed snowdepth from lidar resampled and grid aligned to modelled snow depth grid.

Metric	With Redistribution	Without Redistribution	Lidar
MB (m)	-1.05	-1.12	-
RMSE (m)	1.41	1.44	-
CV (-)	0.61	0.35	0.45

Table 3: Coefficient of variation (CV) for simulated SWE for the regions shown in Figure 1.

Region	With Redistribution	Without Redistribution
Coastal CAN	1.2	1.1
Coastal US	2.6	2.5
Interior CAN	0.6	0.6
Interior US	8.3	8.2
Rockies CAN	2.7	2.6
Rockies US	3.6	3.7

References

Adler, C., P. Wester, I. Bhatt, C. Huggel, G. E. Insarov, M. D. Morecroft, V. Muccione, and A. Prakash (2022), Cross-Chapter Paper 5: Mountains, in *Climate change 2022: Impacts, adaptation and vulnerability*, edited by -O. Pörtner et al., pp. 2273–2318, Cambridge University Press, Cambridge, UK; New York, NY, USA,.

AIRBUS (2020), Copernicus DEM: Copernicus digital elevation model product handbook,

Arnal, L., A. C. Pietroniro, J. W. Pomeroy, V. Fortin, D. R. Casson, T. A. Stadnyk, P. Rokaya, D. Durnford, E. Friesenhan, and M. P. Clark (2023), Towards a coherent flood forecasting framework for Canada: Local to global implications, *Journal of Flood Risk Management*, doi:10.1111/jfr3.12895.

Aubry-Wake, C., D. Pradhananga, and J. W. Pomeroy (2022), Hydrological process controls on streamflow variability in a glacierized headwater basin, *Hydrological Processes*, *36*(10), doi:10.1002/hyp.14731.

Azad, A., M. Jacquelin, A. Buluç, and E. G. Ng (2017), The Reverse Cuthill-McKee Algorithm in Distributed-Memory, *2017 IEEE International Parallel and Distributed Processing Symposium (IPDPS)*, 22–31, doi:10.1109/ipdps.2017.85.

Barnett, T. P., J. C. Adam, and D. P. Lettenmaier (2005), Potential impacts of a warming climate on water availability in snow-dominated regions, *Nature*, *438*(7066), 303–309, doi:10.1038/nature04141.

Bartelt, P., and M. Lehning (2002), A physical SNOWPACK model for the Swiss avalanche warning Part I: numerical model, *Cold Regions Science and Technology*, *35*(3), 123 145, doi:10.1016/s0165-232x(02)00074-5.

Bernhardt, M., and K. Schulz (2010), SnowSlide: A simple routine for calculating gravitational snow transport, *Geophysical Research Letters*, *37*(11), n/a–n/a, doi:10.1029/2010gl043086.

Beven, K. (1989), Changing ideas in hydrology — The case of physically-based models, *Journal of Hydrology*, *105*, 157–172, doi:10.1016/0022-1694(89)90101-7.

Bowling, L. C., J. W. Pomeroy, and D. P. Lettenmaier (2004), Parameterization of Blowing-Snow Sublimation in a Macroscale Hydrology Model, *Journal of Hydrometeorology*, *5*(5), 745–762, doi:10.1175/1525-7541(2004)005<0745:pobsia>2.0.co;2.

Brown, R. D., and R. O. Braaten (1998), Spatial and temporal variability of Canadian monthly snow depths, 1946–1995, *Atmosphere-Ocean*, *36*(1), 37–54, doi:10.1080/07055900.1998.9649605.

Canada, N. R. (n.d.), Natural Resources Canada: Precise Point Positioning Online Tool, [online] Available from: https://webapp.csrs-scrs.nrcan-rncan.gc.ca/geod/tools-outils/ppp.php?locale=en

Chasmer, L., C. Hopkinson, P. Treitz, H. Mccaughey, A. Barr, and A. Black (2008), A lidar-based hierarchical approach for assessing MODIS fPAR, *Remote Sensing of Environment*, *112*(12), 4344–4357, doi:10.1016/j.rse.2008.08.003.

Colditz, R. R., G. L. Saldaña, P. Maeda, J. A. Espinoza, C. M. Tovar, A. V. Hernández, C. Z. Benítez, I. C. López, and R. Ressl (2012), Generation and analysis of the 2005 land cover map for Mexico using 250m MODIS data, *Remote Sensing of Environment*, *123*, 541–552, doi:10.1016/j.rse.2012.04.021.

Conway, J. P., J. W. Pomeroy, W. D. Helgason, and N. J. Kinar (2018), Challenges in modelling turbulent heat fluxes to snowpacks in forest clearings. Challenges in modelling turbulent heat fluxes to snowpacks in forest clearings., *Journal of Hydrometeorology*, doi:10.1175/jhm-d-18-0050.1.

Cuthill, E., and J. McKee (1969), Reducing the bandwidth of sparse symmetric matrices, *Proceedings of the 1969 24th national conference on* -, 157–172, doi:10.1145/800195.805928.

DeBeer, C. M., and J. W. Pomeroy (2010), Simulation of the snowmelt runoff contributing area in a small alpine basin, *Hydrology and Earth System Sciences*, *14*(7), 1205 1219, doi:10.5194/hess-14-1205-2010.

DeBeer, C. M., H. S. Wheater, W. L. Quinton, S. K. Carey, R. E. Stewart, M. D. MacKay, and P. Marsh (2015), The Changing Cold Regions Network: Observation, diagnosis and prediction of environmental change in the Saskatchewan and Mackenzie River Basins, Canada, *Science China Earth Sciences*, *58*(1), 46–60, doi:10.1007/s11430-014-5001-6.

DeBeer, C. M., H. S. Wheater, S. K. Carey, and K. P. Chun (2016), Recent climatic, cryospheric, and hydrological changes over the interior of western Canada: a review and synthesis, *Hydrology and Earth System Sciences*, *20*(4), 1573–1598, doi:10.5194/hess-20-1573-2016.

DeBeer, C. M. et al. (2021), Summary and synthesis of Changing Cold Regions Network (CCRN) research in the interior of western Canada – Part 2: Future change in cryosphere, vegetation, and hydrology, *Hydrology and Earth System Sciences*, *25*(4), 1849–1882, doi:10.5194/hess-25-1849-2021.

Deems, J. S., T. H. Painter, and D. C. Finnegan (2013), Lidar measurement of snow depth: a review, *Journal of Glaciology*, *59*(215), 467–479(13), doi:10.3189/2013jog12j154.

Deschamps-Berger, C., S. Gascoin, D. Shean, H. Besso, A. Guiot, and J. I. López-Moreno (2022), Evaluation of snow depth retrievals from ICESat-2 using airborne laser-scanning data, *The Cryosphere Discussions*, *2022*, 1–17, doi:10.5194/tc-2022-191.

Dornes, P. F., J. W. Pomeroy, a. Pietroniro, and S. K. Careyc (2006), The use of inductive and deductive reasoning to model snowmelt runoff from northern mountain catchments,

Dornes, P. F., J. W. Pomeroy, A. Pietroniro, S. K. Carey, and W. L. Quinton (2008), Influence of landscape aggregation in modelling snow-cover ablation and snowmelt runoff in a sub-arctic mountainous environment, *Hydrological Sciences Journal*, *53*(4), 725–740, doi:10.1623/hysj.53.4.725.

Dozier, J., and J. Frew (1990), Rapid calculation of terrain parameters for radiation modeling from digital elevation data, *IEEE Transactions on Geoscience and Remote Sensing*, *28*(5), 963–969, doi:10.1109/36.58986.

Dubayah, R. et al. (2020), The Global Ecosystem Dynamics Investigation: High-resolution laser ranging of the Earth's forests and topography, *Science of Remote Sensing*, *1*, 100002, doi:10.1016/j.srs.2020.100002.

Ellis, C., J. W. Pomeroy, T. Brown, and J. MacDonald (2010), Simulation of snow accumulation and melt in needleleaf forest environments, *Hydrology and Earth System Sciences*, *14*(6), 925 940, doi:10.5194/hess-14-925-2010.

Ellis, C. R., J. W. Pomeroy, and T. E. Link (2013), Modeling increases in snowmelt yield and desynchronization resulting from forest gap-thinning treatments in a northern mountain headwater basin, *Water Resources Research*, *49*(2), 936 949, doi:10.1002/wrcr.20089.

Endrizzi, S., S. Gruber, M. Dall'Amico, and R. Rigon (2014), GEOtop 2.0: simulating the combined energy and water balance at and below the land surface accounting for soil freezing, snow cover and terrain effects, *Geoscientific Model Development*, *7*(6), 2831 2857, doi:10.5194/gmd-7-2831-2014.

Essery, R. (2015), A factorial snowpack model (FSM 1.0), *Geoscientific Model Development*, *8*(12), 3867 3876, doi:10.5194/gmd-8-3867-2015.

Essery, R., and J. Pomeroy (2004), Vegetation and Topographic Control of Wind-Blown Snow Distributions in Distributed and Aggregated Simulations for an Arctic Tundra Basin, *Journal of Hydrometeorology*, *5*(5), 735–744, doi:10.1175/1525-7541(2004)005<0735:vatcow>2.0.co;2.

Essery, R., N. Rutter, J. Pomeroy, R. Baxter, D. Gustafsson, A. Barr, P. Bartlett, E. Elder, and M. Stahli (2009), SNOWMIP2: An evaluation of forest snow process simulations, *Bulletin of the American Meteorological Society*, *90*(8), 1120–1135, doi:10.1175/2009bams2629.1.

Essery, R., S. Morin, Y. Lejeune, and C. B. Ménard (2013), A comparison of 1701 snow models using observations from an alpine site, *Advances in Water Resources*, *55*, 131–148, doi:10.1016/j.advwatres.2012.07.013.

Etchevers, P. et al. (2004), Validation of the energy budget of an alpine snowpack simulated by several snow models (SnowMIP project), *Annals of Glaciology*, *38*(1), 150–158, doi:10.3189/172756404781814825.

Fang, X., and J. W. Pomeroy (2023), Simulation of the impact of future changes in climate on the hydrology of Bow River headwater basins in the Canadian Rockies, *Journal of Hydrology*, *620*, 129566, doi:10.1016/j.jhydrol.2023.129566.

Fang, X., J. W. Pomeroy, C. R. Ellis, M. K. MacDonald, C. M. DeBeer, and T. Brown (2013), Multi-variable evaluation of hydrological model predictions for a headwater basin in the Canadian Rocky Mountains, *Hydrology and Earth System Sciences*, *17*(4), 1635–1659, doi:10.5194/hess-17-1635-2013.

Flügel, W. A. (1995), Hydrological response units (HRUs) to preserve basin heterogeneity in hydrological modelling using PRMS/MMS-Case study in the Brol basin, Germany.

Forthofer, J. M., B. W. Butler, and N. S. Wagenbrenner (2014), A comparison of three approaches for simulating fine-scale surface winds in support of wildland fire management. Part I. Model formulation and comparison against measurements, *International Journal of Wildland Fire*, *23*(7), 969–981, doi:10.1071/wf12089.

Fortin, V., G. Roy, T. Stadnyk, K. Koenig, N. Gasset, and A. Mahidjiba (2018), Ten Years of Science Based on the Canadian Precipitation Analysis: A CaPA System Overview and Literature Review†, *Atmosphere-Ocean*, *56*(3), 1–19, doi:10.1080/07055900.2018.1474728.

Gascoin, S., O. Hagolle, M. Huc, L. Jarlan, J.-F. Dejoux, C. Szczypta, R. Marti, and R. Sánchez (2015), A snow cover climatology for the Pyrenees from MODIS snow products, *Hydrology and Earth System Sciences*, *19*(5), 2337–2351, doi:10.5194/hess-19-2337-2015.

Hall, D. K., G. A. Riggs, and V. V. Salomonson (1995), Development of methods for mapping global snow cover using moderate resolution imaging spectroradiometer data, *Remote Sensing of Environment*, *54*(2), 127–140, doi:10.1016/0034-4257(95)00137-p.

Hansen, M. C. et al. (2013), High-Resolution Global Maps of 21st-Century Forest Cover Change, *Science*, *342*(6160), 850–853, doi:10.1126/science.1244693.

Harder, P., and J. Pomeroy (2013), Estimating precipitation phase using a psychrometric energy balance method, *Hydrological Processes*, *27*(13), 1901–1914, doi:10.1002/hyp.9799.

Harder, P., M. Schirmer, J. Pomeroy, and W. Helgason (2016), Accuracy of snow depth estimation in mountain and prairie environments by an unmanned aerial vehicle, *The Cryosphere*, *10*(6), 2559–2571, doi:10.5194/tc-10-2559-2016.

Harder, P., W. D. Helgason, and J. W. Pomeroy (2018), Modeling the Snowpack Energy Balance during Melt under Exposed Crop Stubble, *Journal of Hydrometeorology*, *19*(7), 1191–1214, doi:10.1175/jhm-d-18-0039.1.

Harder, P., J. W. Pomeroy, and W. D. Helgason (2020), Improving sub-canopy snow depth mapping with unmanned aerial vehicles: lidar versus structure-from-motion techniques, *The Cryosphere*, *14*(6), 1919–1935, doi:10.5194/tc-14-1919-2020.

Harding, R. J., and J. W. Pomeroy (1996), The Energy Balance of the Winter Boreal Landscape, *Journal of Climate*, *9*(11), 2778–2787, doi:10.1175/1520-0442(1996)009<2778:tebotw>2.0.co;2.

Hatchett, B. J. (2021), Seasonal and Ephemeral Snowpacks of the Conterminous United States, *Hydrology*, *8*(1), 32, doi:10.3390/hydrology8010032.

Havens, S., D. Marks, K. FitzGerald, M. Masarik, A. N. Flores, P. Kormos, and A. Hedrick (2019), Approximating input data to a snowmelt model using Weather Research and Forecasting model outputs in lieu of meteorological measurements, *Journal of Hydrometeorology*, *20*(5), 847–862, doi:10.1175/jhm-d-18-0146.1.

Hawker, L., P. Uhe, L. Paulo, J. Sosa, J. Savage, C. Sampson, and J. Neal (2022), A 30 m global map of elevation with forests and buildings removed, *Environmental Research Letters*, *17*(2), 024016, doi:10.1088/1748-9326/ac4d4f.

Hedstrom, N. R., and J. W. Pomeroy (1997), Accumulation of Intercepted Snow in the Boreal Forest: measurements and modelling, pp. 130 141.

Hopkinson, C., and L. Chasmer (2009), Testing LiDAR models of fractional cover across multiple forest ecozones, *Remote Sensing of Environment*, *113*(1), 275–288, doi:10.1016/j.rse.2008.09.012.

Horton, S., and P. Haegeli (2022), Using snow depth observations to provide insight into the quality of snowpack simulations for regional-scale avalanche forecasting, *The Cryosphere*, *16*(8), 3393–3411, doi:10.5194/tc-16-3393-2022.

Hrachowitz, M., and M. P. Clark (2017), HESS Opinions: The complementary merits of competing modelling philosophies in hydrology, *Hydrology and Earth System Sciences*, *21*(8), 3953 3973, doi:10.5194/hess-21-3953-2017.

Isenburg, M. (n.d.), LAStools - efficient LiDAR processing software, [online] Available from: http://rapidlasso.com/LAStools

Jacobs, J. M., A. G. Hunsaker, F. B. Sullivan, M. Palace, E. A. Burakowski, C. Herrick, and E. Cho (2021), Snow depth mapping with unpiloted aerial system lidar observations: a case study in Durham, New Hampshire, United States, *The Cryosphere*, *15*(3), 1485–1500, doi:10.5194/tc-15-1485-2021.

Jenicek, M., J. Seibert, M. Zappa, M. Staudinger, and T. Jonas (2016), Importance of maximum snow accumulation for summer low flows in humid catchments, *Hydrology and Earth System Sciences*, *20*(2), 859–874, doi:10.5194/hess-20-859-2016.

Kapos, V., J. Rhind, M. Edwards, M. F. Price, and C. Ravilious (2000), Developing a map of the world's mountain forests, in *Forests in sustainable mountain development: A state-of knowledge report for 2000*.

Karypis, G., and V. Kumar (1998), A Fast and High Quality Multilevel Scheme for Partitioning Irregular Graphs, *SIAM Journal on Scientific Computing*, *20*(1), 359–392, doi:10.1137/s1064827595287997.

Kienzle, S. W. (2011), Effects of area under-estimations of sloped mountain terrain on simulated hydrological behaviour: a case study using the ACRU model, *Hydrological Processes*, *25*(8), 1212–1227, doi:10.1002/hyp.7886.

Krinner, G. et al. (2018), ESM-SnowMIP: assessing snow models and quantifying snow-related climate feedbacks, *Geoscientific Model Development*, *11*(12), 5027–5049, doi:10.5194/gmd-11-5027-2018.

Krogh, S. A., J. W. Pomeroy, and J. McPhee (2015), Physically Based Mountain Hydrological Modeling Using Reanalysis Data in Patagonia, *Journal of Hydrometeorology*, *16*(1), 172–193, doi:10.1175/jhm-d-13-0178.1.

Kumar, M., D. Marks, J. Dozier, M. Reba, and A. Winstral (2013), Evaluation of distributed hydrologic impacts of temperature-index and energy-based snow models, *Advances in Water Resources*, *56*, 77 89, doi:10.1016/j.advwatres.2013.03.006.

Kunkel, K. E. (1989), Simple Procedures for Extrapolation of Humidity Variables in the Mountainous Western United States, *Journal of Climate*, *2*(7), 656–670, doi:10.1175/1520-0442(1989)002<0656:spfeoh>2.0.co;2.

Lapen, D. R., and L. W. Martz (1993), The measurement of two simple topographic indices of wind sheltering-exposure from raster digital elevation models, *Computers & Geosciences*, *19*(6), 769–779, doi:10.1016/0098-3004(93)90049-b.

Latifovic, R., C. Homer, R. Ressl, D. Pouliot, S. N. Hossain, R. R. Colditz, I. Olthof, C. P. Giri, and A. Victoria (2016), North American Land-Change Monitoring System, in *Remote sensing of land use and land cover*, p. 303.

Li, Y., F. Li, D. Shangguan, and Y. Ding (2021), A new global gridded glacier dataset based on the Randolph Glacier Inventory version 6.0, *Journal of Glaciology*, *67*(264), 773–776, doi:10.1017/jog.2021.28.

Liston, G. E., and K. Elder (2006), A Meteorological Distribution System for High-Resolution Terrestrial Modeling (MicroMet), *Journal of Hydrometeorology*, *7*(2), 217–234, doi:10.1175/jhm486.1.

Lumbrazo, C., A. Bennett, W. R. Currier, B. Nijssen, and J. Lundquist (2022), Evaluating Multiple Canopy-Snow Unloading Parameterizations in SUMMA With Time-Lapse Photography Characterized by Citizen Scientists, *Water Resources Research*, *58*(6), doi:10.1029/2021wr030852.

Lundquist, J., M. Hughes, E. Gutmann, and S. Kapnick (2019), Our skill in modeling mountain rain and snow is bypassing the skill of our observational networks Our skill in modeling mountain rain and snow is bypassing the skill of our observational networks, *Bulletin of the American Meteorological Society*, *100*(12), 2473–2490, doi:10.1175/bams-d-19-0001.1.

Lundquist, J. D., S. Dickerson-Lange, E. Gutmann, T. Jonas, C. Lumbrazo, and D. Reynolds (2021), Snow interception modeling: Isolated observations have led to many land surface models lacking appropriate temperature sensitivities, *Hydrological Processes*, doi:10.1002/hyp.14274.

MacDonald, M. K., J. W. Pomeroy, and A. Pietroniro (2009), Parameterizing redistribution and sublimation of blowing snow for hydrological models: tests in a mountainous subarctic catchment, *Hydrological Processes*, *23*(18), 2570–2583, doi:10.1002/hyp.7356.

MacDonald, M. K., J. W. Pomeroy, and A. Pietroniro (2010), On the importance of sublimation to an alpine snow mass balance in the Canadian Rocky Mountains, *Hydrology and Earth System Sciences*, *14*(7), 1401–1415, doi:10.5194/hess-14-1401-2010.

MacDonald, M. K., J. W. Pomeroy, and R. L. H. Essery (2018), Water and energy fluxes over northern prairies as affected by chinook winds and winter precipitation, *Agricultural and Forest Meteorology*, *248*, 372–385, doi:10.1016/j.agrformet.2017.10.025.

Mai, J., K. C. Kornelsen, B. A. Tolson, V. Fortin, N. Gasset, D. Bouhemhem, D. Schäfer, M. Leahy, F. Anctil, and P. Coulibaly (2019), The Canadian Surface Prediction Archive (CaSPAr): A Platform to Enhance Environmental Modeling in Canada and Globally The Canadian Surface Prediction Archive (CaSPAr): A Platform to Enhance Environmental Modeling in Canada and Globally, *Bulletin of the American Meteorological Society*, *101*(3), E341–E356, doi:10.1175/bams-d-19-0143.1.

Marks, D., and A. Winstral (2001), Comparison of Snow Deposition, the Snow Cover Energy Balance, and Snowmelt at Two Sites in a Semiarid Mountain Basin, *Journal of Hydrometeorology*, *2*(3), 213–227, doi:10.1175/1525-7541(2001)002<0213:cosdts>2.0.co.

Marsh, C. B., J. W. Pomeroy, and R. J. Spiteri (2012), Implications of mountain shading on calculating energy for snowmelt using unstructured triangular meshes, *Hydrological Processes*, *26*(12), 1767–1778, doi:10.1002/hyp.9329.

Marsh, C. B., R. J. Spiteri, J. W. Pomeroy, and H. S. Wheater (2018), Multi-objective unstructured triangular mesh generation for use in hydrological and land surface models, *Computers & Geosciences*, *119*, 49–67, doi:10.1016/j.cageo.2018.06.009.

Marsh, C. B., J. W. Pomeroy, R. J. Spiteri, and H. S. Wheater (2020a), A Finite Volume Blowing Snow Model for Use With Variable Resolution Meshes, *Water Resources Research*, *56*(2), 1–28, doi:10.1029/2019wr025307.

Marsh, C. B., J. W. Pomeroy, and H. S. Wheater (2020b), The Canadian Hydrological Model (CHM) v1.0: a multi-scale, multi-extent, variable-complexity hydrological model – design and overview, *Geoscientific Model Development*, *13*(1), 225–247, doi:10.5194/gmd-13-225-2020.

Marsh, C. B., P. Harder, and J. W. Pomeroy (2023a), Validation of FABDEM, a global bare-earth elevation model, against UAV-lidar derived elevation in a complex forested mountain catchment, *Environmental Research Communications*, doi:10.1088/2515-7620/acc56d.

Marsh, C. B., V. Vionnet, and J. W. Pomeroy (2023b), Windmapper: An Efficient Wind Downscaling Method for Hydrological Models, *Water Resources Research*, *59*(3), doi:10.1029/2022wr032683.

Marsh, P., and J. W. Pomeroy (1996), Meltwater Fluxes at an Arctic Forest-tundra Site, *Hydrological Processes*, *10*(10), 1383–1400, doi:10.1002/(sici)1099-1085(199610)10:10<1383::aid-hyp468>3.0.co;2-w.

Marty, Ch., R. Philipona, C. Fröhlich, and A. Ohmura (2002), Altitude dependence of surface radiation fluxes and cloud forcing in the alps: results from the alpine surface radiation budget network, *Theoretical and Applied Climatology*, *72*(3), 137–155, doi:10.1007/s007040200019.

Mazzotti, G., R. Essery, C. Webster, J. Malle, and T. Jonas (2020a), Process-Level Evaluation of a Hyper-Resolution Forest Snow Model Using Distributed Multisensor Observations, *Water Resources Research*, *56*(9), doi:10.1029/2020wr027572.

Mazzotti, G., R. Essery, C. D. Moeser, and T. Jonas (2020b), Resolving small-scale forest snow patterns using an energy-balance snow model with a 1-layer canopy, *Water Resources Research*, doi:10.1029/2019wr026129.

Milbrandt, J. A., S. Bélair, M. Faucher, M. Vallée, M. L. Carrera, and A. Glazer (2016), The Pan-Canadian High Resolution (2.5 km) Deterministic Prediction System, *Weather and Forecasting*, *31*(6), 1791–1816, doi:10.1175/waf-d-16-0035.1.

Mo, R., M. M. Brugman, J. A. Milbrandt, J. Goosen, Q. Geng, C. Emond, J. Bau, and A. Erfani (2019), Impacts of Hydrometeor Drift on Orographic Precipitation: Two Case Studies of Landfalling Atmospheric Rivers in British Columbia, Canada Impacts of Hydrometeor Drift on Orographic Precipitation: Two Case Studies of Landfalling Atmospheric Rivers in British Columbia, Canada, *Weather and Forecasting*, *34*(5), 1211–1237, doi:10.1175/waf-d-18-0176.1.

Mosier, T. M., D. F. Hill, and K. V. Sharp (2016), How Much Cryosphere Model Complexity is Just Right? Exploration Using the Conceptual Cryrosphere Hydrology Framework, *The Cryosphere Discussions*, (February), 1–33, doi:10.5194/tc-2016-17.

Mott, R., M. Schirmer, M. Bavay, T. Grünewald, and M. Lehning (2010), Understanding snow-transport processes shaping the mountain snow-cover, *The Cryosphere*, *4*(4), 545–559, doi:10.5194/tc-4-545-2010.

Mott, R., V. Vionnet, and T. Grünewald (2018), The Seasonal Snow Cover Dynamics: Review on Wind-Driven Coupling Processes, *Frontiers in Earth Science*, *6*, 197, doi:10.3389/feart.2018.00197.

Mott, R., A. Wolf, M. Kehl, H. Kunstmann, M. Warscher, and T. Grünewald (2019), Avalanches and micrometeorology driving mass and energy balance of the lowest perennial ice field of the Alps: a case study, *The Cryosphere*, *13*(4), 1247–1265, doi:10.5194/tc-13-1247-2019.

Mott, R., A. Winstral, B. Cluzet, N. Helbig, J. Magnusson, G. Mazzotti, L. Quéno, M. Schirmer, C. Webster, and T. Jonas (2023), Operational snow-hydrological modeling for Switzerland, *Frontiers in Earth Science*, *11*, 1228158, doi:10.3389/feart.2023.1228158.

Musselman, K. N., and J. W. Pomeroy (2016), Estimation of needle-leaf canopy and trunk temperatures and longwave contribution to melting snow, *Journal of Hydrometeorology*, *18*(2), 555–572, doi:10.1175/jhm-d-16-0111.1.

Musselman, K. N., J. W. Pomeroy, R. L. H. Essery, and N. Leroux (2015a), Impact of windflow calculations on simulations of alpine snow accumulation, redistribution and ablation, *Hydrological Processes*, *29*(18), 3983–3999, doi:10.1002/hyp.10595.

Musselman, K. N., J. W. Pomeroy, and T. E. Link (2015b), Variability in shortwave irradiance caused by forest gaps: Measurements, modelling, and implications for snow energetics, *Agricultural and Forest Meteorology*, *207*, 69–82, doi:10.1016/j.agrformet.2015.03.014.

Musselman, K. N., M. P. Clark, C. Liu, K. Ikeda, and R. Rasmussen (2017), Slower snowmelt in a warmer world, *Nature Climate Change*, *7*(3), 214 219, doi:10.1038/nclimate3225.

Nazemi, A., H. S. Wheater, K. P. Chun, and A. Elshorbagy (2013), A stochastic reconstruction framework for analysis of water resource system vulnerability to climate-induced changes in river flow regime, *Water Resources Research*, *49*(1), 291–305, doi:10.1029/2012wr012755.

Neuenschwander, A. L., K. L. Pitts, B. P. Jelley, J. Robbins, B. Klotz, S. C. Popescu, R. F. Nelson, D. Harding, D. Pederson, and R. Sheridan. (2021), ATLAS/ICESat-2 L3A Land and Vegetation Height, Version 4, *Boulder, Colorado USA. NASA National Snow and Ice Data Center Distributed Active Archive Center*, doi:10.5067/atlas/atl08.004.

Painter, S. L., E. T. Coon, A. L. Atchley, M. Berndt, R. Garimella, J. D. Moulton, D. Svyatskiy, and C. J. Wilson (2016a), Integrated surface/subsurface permafrost thermal hydrology: Model formulation and proof-of-concept simulations, *Water Resources Research*, *52*(8), 6062–6077, doi:10.1002/2015wr018427.

Painter, T. H. et al. (2016b), The Airborne Snow Observatory: Fusion of scanning lidar, imaging spectrometer, and physically-based modeling for mapping snow water equivalent and snow albedo, *Remote Sensing of Environment*, *184*, 139–152, doi:10.1016/j.rse.2016.06.018.

Pelto, B. M., B. Menounos, and S. J. Marshall (2019), Multi-year evaluation of airborne geodetic surveys to estimate seasonal mass balance, Columbia and Rocky Mountains, Canada, *The Cryosphere*, *13*(6), 1709–1727, doi:10.5194/tc-13-1709-2019.

Pomeroy, J., X. Fang, and C. Ellis (2012), Sensitivity of snowmelt hydrology in Marmot Creek, Alberta, to forest cover disturbance, *Hydrological Processes*, *26*(12), 1891–1904, doi:10.1002/hyp.9248.

Pomeroy, J. W., and D. M. Gray (1995), *Snowcover: Accumulation, relocation and management*, Environment canada, 1st ed., Environment Canada.

Pomeroy, J. W., and L. Li (2000), Prairie and arctic areal snow cover mass balance using a blowing snow model, *Journal of Geophysical Research: Atmospheres*, *105*(D21), 26619–26634, doi:10.1029/2000jd900149.

Pomeroy, J. W., D. M. Gray, and P. G. Landine (1993), The Prairie Blowing Snow Model: characteristics, validation, operation, *Journal of Hydrology*, *144*(1-4), 165–192, doi:10.1016/0022-1694(93)90171-5.

Pomeroy, J. W., J. Parviainen, N. Hedstrom, and D. M. Gray (1998), Coupled modelling of forest snow interception and sublimation, *Hydrological Processes*, *12*(15), 2317–2337, doi:10.1002/(sici)1099-1085(199812)12:15<2317::aid-hyp799>3.0.co;2-x.

Pomeroy, J. W., B. Toth, R. J. Granger, N. R. Hedstrom, and R. L. H. Essery (2003), Variation in surface energetics during snowmelt in a subarctic mountain catchment, *Journal of Hydrometeorology*, *4*(4), 702–719, doi:10.1175/1525-7541(2003)004<0702:viseds>2.0.co;2.

Pomeroy, J. W., A. Rowlands, J. Hardy, T. Link, D. Marks, R. Essery, J. E. Sicart, and C. Ellis (2007), Spatial Variability of Shortwave Irradiance for Snowmelt in Forests, *Journal of Hydrometeorology*, *9*(6), 1482, doi:10.1175/2008jhm867.1.

Pomeroy, J. W., D. Marks, T. Link, C. Ellis, J. Hardy, A. Rowlands, and R. Granger (2009), The impact of coniferous forest temperature on incoming longwave radiation to melting snow, *Hydrological Processes*, *23*(17), 2513–2525, doi:10.1002/hyp.7325.

Pomeroy, J. W. et al. (2022), The cold regions hydrological modelling platform for hydrological diagnosis and prediction based on process understanding, *Journal of Hydrology*, *615*(Hydrology and Earth System Science 26 21 2022), 128711, doi:10.1016/j.jhydrol.2022.128711.

Potapov, P. et al. (2021), Mapping global forest canopy height through integration of GEDI and Landsat data, *Remote Sensing of Environment*, *253*, 112165, doi:10.1016/j.rse.2020.112165.

Pradhananga, D., and J. W. Pomeroy (2022), Diagnosing changes in glacier hydrology from physical principles using a hydrological model with snow redistribution, sublimation, firnification and energy balance ablation algorithms, *Journal of Hydrology*, *608*, 127545, doi:10.1016/j.jhydrol.2022.127545.

Quéno, L., V. Vionnet, I. Dombrowski-Etchevers, M. Lafaysse, M. Dumont, and F. Karbou (2016), Snowpack modelling in the Pyrenees driven by kilometric-resolution meteorological forecasts, *The Cryosphere*, *10*(4), 1571–1589, doi:10.5194/tc-10-1571-2016.

Quéno, L., V. Vionnet, F. Cabot, D. Vrécourt, and I. Dombrowski-Etchevers (2018), Forecasting and modelling ice layer formation on the snowpack due to freezing precipitation in the Pyrenees, *Cold Regions Science and Technology*, *146*, 19–31, doi:10.1016/j.coldregions.2017.11.007.

Raderschall, N., M. Lehning, and C. Schär (2008), Fine-scale modeling of the boundary layer wind field over steep topography, *Water Resources Research*, *44*(9), 1–18, doi:10.1029/2007wr006544.

Rasmussen, R. et al. (2012), How Well Are We Measuring Snow: The NOAA/FAA/NCAR Winter Precipitation Test Bed, *Bulletin of the American Meteorological Society*, *93*(6), 811–829, doi:10.1175/bams-d-11-00052.1.

Rasouli, K., J. W. Pomeroy, and P. H. Whitfield (2022), The sensitivity of snow hydrology to changes in air temperature and precipitation in three North American headwater basins, *Journal of Hydrology*, *606*, 127460, doi:10.1016/j.jhydrol.2022.127460.

Reba, M. L., T. E. Link, D. Marks, and J. Pomeroy (2009), An assessment of corrections for eddy covariance measured turbulent fluxes over snow in mountain environments, *Water Resources Research*, *45*(4), n/a n/a, doi:10.1029/2008wr007045.

Rupp, K., P. Tillet, F. Rudolf, J. Weinbub, A. Morhammer, T. Grasser, A. Jüngel, and S. Selberherr (2016), ViennaCL—Linear Algebra Library for Multi- and Many-Core Architectures, *SIAM Journal on Scientific Computing*, *38*(5), S412–S439, doi:10.1137/15m1026419.

Rutter, N. et al. (2019), Effect of snow microstructure variability on Ku-band radar snow water equivalent retrievals, *The Cryosphere*, *13*(11), 3045–3059, doi:10.5194/tc-13-3045-2019.

Sandells, M. et al. (2021), Community Development of the Snow Microwave Radiative Transfer Model for Passive, Active and Altimetry Observations of the Cryosphere, *2021 IEEE International Geoscience and Remote Sensing Symposium IGARSS*, *00*, 852–855, doi:10.1109/igarss47720.2021.9553580.

Schirmer, M., and B. Jamieson (2015), Verification of analysed and forecasted winter precipitation in complex terrain, *The Cryosphere*, *9*(2), 587–601, doi:10.5194/tc-9-587-2015.

Shea, J. M., S. J. Marshall, and J. M. Livingston (2004), Glacier Distributions and Climate in the Canadian Rockies, *Arctic, Antarctic, and Alpine Research*, *36*(2), 272–279, doi:10.1657/1523-0430(2004)036[0272:gdacit]2.0.co;2.

Sicart, J. E., J. W. Pomeroy, R. L. H. Essery, and D. Bewley (2006), Incoming longwave radiation to melting snow: observations, sensitivity and estimation in Northern environments, *Hydrological Processes*, *20*(17), 3697–3708, doi:10.1002/hyp.6383.

Sobie, S. R., and T. Q. Murdock (2021), Projections of snow water equivalent using a process-based energy balance snow model in southwestern British Columbia, *Journal of Applied Meteorology and Climatology*, doi:10.1175/jamc-d-20-0260.1.

Sturm, M., M. A. Goldstein, and C. Parr (2017), Water and life from snow: A trillion dollar science question, *Water Resources Research*, *53*(5), 3534–3544, doi:10.1002/2017wr020840.

Sun, N., H. Yan, M. S. Wigmosta, L. R. Leung, R. Skaggs, and Z. Hou (2019), Regional Snow Parameters Estimation for Large-Domain Hydrological Applications in the Western United States, *Journal of Geophysical Research: Atmospheres*, *124*(10), 5296–5313, doi:10.1029/2018jd030140.

Team, T. Trilinos Project (2020 (acccessed May 22, 2020)), *The Trilinos Project Website*. [online] Available from: https://trilinos.github.io

Tedesco, M., C. Derksen, J. S. Deems, and J. L. Foster (2014), Remote sensing of snow depth and snow water equivalent, in *Remote sensing of the cryosphere*, edited by M. Tedesco, pp. 73–98.

Tsang, L. et al. (2022), Review article: Global monitoring of snow water equivalent using high-frequency radar remote sensing, *The Cryosphere*, *16*(9), 3531–3573, doi:10.5194/tc-16-3531-2022.

Vionnet, V., E. Martin, V. Masson, G. Guyomarc'H, F. Naaim-Bouvet, A. Prokop, Y. Durand, and C. Lac (2014), Simulation of wind-induced snow transport and sublimation in alpine terrain using a fully coupled snowpack/atmosphere model, *Cryosphere*, *8*(2), 395–415, doi:10.5194/tc-8-395-2014.

Vionnet, V., C. Mortimer, M. Brady, L. Arnal, and R. Brown (2021a), Canadian historical Snow Water Equivalent dataset (CanSWE, 1928–2020), *Earth System Science Data*, *13*(9), 4603–4619, doi:10.5194/essd-13-4603-2021.

Vionnet, V., C. B. Marsh, B. Menounos, S. Gascoin, N. E. Wayand, J. Shea, K. Mukherjee, and J. W. Pomeroy (2021b), Multi-scale snowdrift-permitting modelling of mountain snowpack, *The Cryosphere*, *15*(2), 743–769, doi:10.5194/tc-15-743-2021.

Viviroli, D., M. Kummu, M. Meybeck, M. Kallio, and Y. Wada (2020), Increasing dependence of lowland populations on mountain water resources, *Nature Sustainability*, *3*(11), 917–928, doi:10.1038/s41893-020-0559-9.

Wagenbrenner, N. S., J. M. Forthofer, W. G. Page, and B. W. Butler (2019), Development and Evaluation of a Reynolds-Averaged Navier–Stokes Solver in WindNinja for Operational Wildland Fire Applications, *Atmosphere*, *10*(11), 672, doi:10.3390/atmos10110672.

Wayand, N. E., C. B. Marsh, J. M. Shea, and J. W. Pomeroy (2018), Globally scalable alpine snow metrics, *Remote Sensing of Environment*, *213*, 61–72, doi:10.1016/j.rse.2018.05.012.

Whitfield, P. H., P. D. A. Kraaijenbrink, K. R. Shook, and J. W. Pomeroy (2021), The spatial extent of hydrological and landscape changes across the mountains and prairies of Canada in the Mackenzie and Nelson River basins based on data from a warm-season time window, *Hydrology and Earth System Sciences*, *25*(5), 2513–2541, doi:10.5194/hess-25-2513-2021.

Winstral, A., D. Marks, and R. Gurney (2009), An efficient method for distributing wind speeds over heterogeneous terrain, *Hydrological Processes*, *23*(17), 2526–2535, doi:10.1002/hyp.7141.

Yamazaki, D., D. Ikeshima, J. Sosa, P. D. Bates, G. H. Allen, and T. M. Pavelsky (2019), MERIT Hydro: A High-Resolution Global Hydrography Map Based on Latest Topography Dataset, *Water Resources Research*, *55*(6), 5053–5073, doi:10.1029/2019wr024873.

Yan, H., N. Sun, M. Wigmosta, R. Skaggs, Z. Hou, and R. Leung (2018), Next-Generation Intensity-Duration-Frequency Curves for Hydrologic Design in Snow-Dominated Environments, *Water Resources Research*, *54*(2), 1093–1108, doi:10.1002/2017wr021290.